# Convection-generated gravity waves in the tropical lower stratosphere from Aeolus wind profiling, GNSS-RO and ERA5 reanalysis

Mathieu Ratynski<sup>1,a,\*</sup>, Sergey Khaykin<sup>1</sup>, Alain Hauchecorne<sup>1</sup>, M. Joan Alexander<sup>2</sup>, Alexis Mariaccia<sup>3</sup>, Philippe Keckhut<sup>1</sup> and Antoine Mangin<sup>4</sup>

Correspondence to: Mathieu Ratynski (mathieu.ratynski@estaca.eu)

Abstract. The European Space Agency's Aeolus satellite, equipped with the Atmospheric LAser Doppler INstrument (ALADIN), provides near-global wind profiles from the surface to about 30 km altitude. These wind measurements enable the investigation of atmospheric dynamics, including gravity waves (GWs) in the upper troposphere and lower stratosphere (UTLS). This study analyzes ALADIN wind observations and ERA5 reanalysis, by deriving GWs kinetic energy (Ek) distributions, examining their temporal and spatial variability throughout the tropical UTLS. A prominent hotspot of enhanced GW activity is identified by Aeolus, migrating from the Indian Ocean in Boreal Summer to the Maritime Continent in Boreal Winter, closely matching outgoing longwave radiation minima and thus highlighting convective origins. Results show that ERA5 consistently underestimates Ek in convective regions, especially over the Indian Ocean, where conventional wind measurements are sparse. Additional comparisons with Global Navigation Satellite System Radio Occultation (GNSS-RO) measurements of GW potential energy (Ep) corroborate these findings and suggest significant underrepresentation of convection-driven wave activity in reanalyses. A multi-instrumental exploratory analysis also allows to verify the empirical grounding of the established Ek to Ep ratio. By providing direct wind measurements in otherwise data-sparse regions, Aeolus offers a valuable dataset for evaluating and potentially improving the representation of GWs in reanalyses, particularly in remote tropical areas. The combination of Aeolus and GNSS-RO data allows for an observationally-based examination of the partitioning between kinetic and potential energy, highlighting discrepancies with reanalysis products that could inform future model parameterization development.

<sup>&</sup>lt;sup>1</sup>Laboratoire Atmosphère Milieux et Observation Spatiales (LATMOS), UVSQ, CNRS, Univeristé Paris Saclay, Guyancourt, France

<sup>&</sup>lt;sup>2</sup>NorthWest Research Associate, Boulder, CO, US

<sup>&</sup>lt;sup>3</sup>Program in Atmospheric and Oceanic Sciences, Princeton University, Princeton, New Jersey, United States

<sup>&</sup>lt;sup>4</sup>ACRI-ST, 260 Route du Pin Montard, Sophia-Antipolis, Biot 06410, France

anow at : Rosenstiel School of Marine and Atmospheric Science, University of Miami, Coral Gables, Florida, United States

#### 1. Introduction

6

11

14

19

27

- 2 Atmospheric reanalyses like ERA5, a global atmospheric dataset produced by the European Centre for Medium-range Weather
- 3 Forecasts (ECMWF), are essential for climate assessments and atmospheric research (Hersbach et al., 2020). By integrating
- observational data with state-of-the-art general circulation models and data assimilation methods, reanalyses provide 4
- comprehensive atmospheric snapshots for a variety of meteorological research (Muñoz-Sabater et al., 2021). 5

7 However, one significant limitation of these datasets, including ERA5, is their reliance predominantly on temperature

- measurements for data assimilation, with wind measurements being notably sparse (Campos et al., 2022; Podglaien et al., 8
- 9 2014). Because of this, ERA5 tends to underestimate low-level wind speeds in certain regions, compared to radiosonde
- 10 measurements (Munday et al., 2022). Having said that, only a relatively few radiosonde and cloud-tracked wind measurements
  - directly constrain wind variability; Radiosonde measurements are notably sparse over oceans, as they are typically launched
- 12 from land-based stations, leaving vast oceanic regions under-sampled (Baker et al., 2014; Ladstädter et al., 2011). While some
- 13 ship-based radiosonde launches occur, they are infrequent and cover limited areas. Satellite cloud-tracking methods, such as
- Atmospheric Motion Vectors (AMVs), provide wind data by tracking cloud movements (Bedka et al., 2009). However, these
- methods have limitations: they cannot retrieve wind profiles in clear-sky conditions and often lack detailed vertical resolution. 15
- This results in significant observational gaps in wind measurements over oceans and clear-sky regions. This limitation is 16
- 17 particularly critical when considering atmospheric waves, such as gravity waves, which manifest themselves in temperature
- 18 and wind vertical profiles.
- Gravity waves (GW) play a crucial role in the dynamics of the Earth's atmosphere. Generated by mechanisms such as flow 20
- over orography, convection, and flow deformation, these waves are instrumental in transporting momentum and energy, 21
- 22 influencing atmospheric regions far from their origin points (Fritts and Alexander, 2003). While Rossby waves are well
- represented due to their quasi-geostrophic nature, divergent wave modes like gravity waves, Kelvin waves, Rossby-gravity 23
- waves, and inertia-gravity waves are not sufficiently characterized and must often be parametrized internally by the models
- (Plougonven and Zhang, 2014). The underrepresentation of gravity waves with long horizontal and short vertical scales in
- 25
- ERA5 has been highlighted previously (Bramberger et al., 2022). 26
- 28 For the study period from June 2019 to August 2022 For the study period. ERA5 utilizes the non-orographic gravity wave drag
- (GWD) scheme described by Orr et al., (2010), which is based on a spectral approach (Scinocca, 2003). This scheme does not 29
- 30 explicitly resolve convectively generated waves based on model-diagnosed convection; instead, it launches a globally uniform
- 31 and constant spectrum of waves from the troposphere. The momentum deposition occurs as these waves propagate vertically
- and interact with the resolved flow via critical-level filtering and nonlinear dissipation. While this parameterization improves

the middle atmosphere climate compared to simpler schemes, evaluations have shown it has limitations in fully capturing the required wave forcing, particularly for the Quasi-Biennial Oscillation (QBO) in the tropics (Pahlavan et al., 2021).

33

34 35

44

50

60

Furthermore, even with improvements in reanalysis products, challenges in accurately representing tropical winds persist. 36 37 Studies of previous-generation reanalyses identified significant errors in tropical regions (Podglajen et al., 2014), and recent 38 work shows that even ERA5's accuracy is highly site-dependent, with notable errors in locations influenced by warm currents (Campos et al., 2022). This is compounded by difficulties in data assimilation systems, such as 4-D var and perfect model 39 scenarios, which struggle to extract circulation information from high-resolution temperature data (Žagar et al., 2004). Despite 40 41 advancements in the quality of tropical forecasts and analyses, the evidence suggests that radio occultation (RO) data could 42 potentially enable effective long-term monitoring of wind fields globally (Danzer et al., 2023). However, the overall lack of direct wind observations continues to pose significant challenges (Baker et al., 2014). 43

Historically, most GW studies have relied on ground-based or single-use instruments like radiosondes (Zhang and Yi, 2005), rockets (Wüst and Bittner, 2008), or global coverage measurements from the Global Navigation Satellite System Radio Occultation (GNSS-RO). While GNSS-RO provides high-resolution temperature profiling, effectively characterizing GW potential energy (Ep) (Fröhlich et al., 2007; Khaykin et al., 2015; Schmidt et al., 2016), it does not capture kinetic energy (Ek), which requires precise wind profiling.

In an effort to bridge many gaps within the observational world, the 2018 launch of the European Space Agency's Aeolus 51 52 satellite changed our ability to capture atmospheric dynamics, particularly in the upper troposphere and lower stratosphere 53 (UTLS). The UTLS is a region marked by a dramatic increase in static stability at the tropopause, where gravity waves are 54 refracted to shorter vertical wavelengths (Dhaka et al., 2006; Geldenhuys et al., 2023). These waves with short vertical 55 wavelengths (typically 2-10 km) are primarily lower-frequency gravity waves, as dictated by the dispersion relation, and exhibit relatively large amplitude wind variability. The Aeolus satellite, equipped with its Atmospheric LAser Doppler 56 INstrument (ALADIN), is able to measure global wind profiles up to an altitude of 30 km, providing insights into the behavior 57 58 of gravity waves with vertical wavelengths down to ~1.5-2 km in these critical atmospheric layers (Banyard et al., 2021; 59 Rennie et al., 2021; Ratynski et al., 2023).

In this context, this study aims at utilizing Aeolus's global wind profiling capabilities to derive a tropics-wide distribution and variability of the kinetic energy of gravity waves, addressing a gap not typically captured in ERA5 reanalysis. By comparing direct measurements with ERA5 data, we reveal certain limitations in the reanalysis's ability to represent tropical gravity wave dynamics. We will look at the most recent reprocessed Aeolus baseline 2B16, providing data from June 2019 to August 2022. Additionally, our study aims at exploring a broader set of analyses, aiming to contextualize the Aeolus wind observations within a multi-instrument framework. By comparing Aeolus-derived kinetic energy of GWs with the potential energy estimates

from GNSS-RO, we assess the consistency of independent data sources and examine the ratio of kinetic to potential energy in real-world atmospheric conditions. With this study, we provide the first observationally-based, tropics-wide estimate of gravity wave kinetic energy from June 2019 to August 2022, directly linking its variability to deep convective sources.

The paper will be organized as follows: In Sect. 2, we will discuss the data as well as the methods. It includes a description of the Aeolus, ERA5 and the GNSS-RO datasets, but also explains the horizontal detrending method with its potential and limitations. In Sect. 3, we will analyze the wave activity in terms of kinetic energy using Aeolus Rayleigh wind profiling and directly comparing it with ERA5. Additionally, in Sect. 4, we broaden our analyses to contextualize Aeolus observations against GNSS-RO data and criticize the ratio between both elements. Finally, the results are discussed in Sect. 5, followed by the conclusions in Sect. 6

The Aeolus satellite, with its ALADIN Doppler wind lidar, orbited Earth at a 97-degree inclination and 320 km altitude. Its

#### 77 2. Data and Methods

70

79

93

## 2.1 Instruments and Datasets

80 data consists of 24 vertical range bins that divide the atmosphere, allowing wind profiling between 0 and 30 km. Laser pulses and two receivers-Rayleigh and Mie channels-detect the atmosphere's Doppler shifts through molecular and particle 81 82 backscatter, respectively. The data, organized into atmospheric scenes, cloudy or clear, has an 87 km along-track integration 83 and a vertical resolution varying between 0.25 to 2 km. Within the tropical UTLS region of this study, the vertical bin size is typically between 0.5 and 1.5 km. The distribution of these range bins is determined by a dedicated range bin setting (RBS), 84 85 which varies geographically to meet different observational goals, with distinct configurations routinely used for the tropics, extratropics, and polar regions. which can be adjusted to cater to specific needs, such as enhanced sampling at certain heights. 86 87 This study uses the Level 2B Rayleigh clear product from June 2019 to August 2022, with the latest Baseline 2B16 at the time of submission, offering the horizontal line of sight (HLOS) wind components. The HLOS wind speed is derived using Aeolus 88 NWP Impact Experiments guidance, with the vertical wind speed assumed to be negligible. A complete description of the 89 90 instrument, its measurement principles, range bin settings, and data products can be found in Rennie and Isaksen. (2024). The angle  $\theta$  denotes the azimuth of the target-to-satellite pointing vector, being around 100.5° over the tropics. When injecting the 91 92 azimuth value into Eq. 1, it becomes apparent that the HLOS wind over the tropics is quasi-zonal.

94 
$$v_{HLOS} = -u \sin(\theta) - v \cos(\theta)$$
 (1)

96 The ERA5 reanalysis dataset, a ECMWF product, offers comprehensive atmospheric, land-surface, and ocean-wave
97 parameters at hourly resolution and global coverage (Hersbach et al., 2020). Its exceptional horizontal resolution of

approximately 33 km at the equator (corresponding to 0.3° latitude/longitude), the best among widely used reanalysis products, enables it to resolve gravity waves with horizontal wavelengths as small as ~100 km (Wright and Hindley, 2018, their table 1). The data products used in this study were retrieved from the ECMWF archive on a regular 0.25° x 0.25° latitude-longitude grid. Additionally, its higher vertical resolution in the troposphere, with 137 vertical levels reaching up to 0.01 hPa, makes it particularly adept at capturing gravity waves with vertical wavelengths down to ~1-2 km. ERA5 also incorporates advanced modelling features such as sponge layers and hyperdiffusion to attenuate artificial wave reflections and stabilize the model numerically, allowing for efficient modelling of large-scale phenomena, notably simulating gravity waves with wavelengths greater than 400 km (Stephan and Mariaccia., 2021). It is therefore the best candidate to use as a benchmark for Aeolus' 106 performances. For representing sub-grid scale gravity waves, the ERA5 configuration used in this study employs a nonorographic GWD parameterization that is not directly forced by model-diagnosed convection (Orr et al., 2010). Instead, the scheme launches a globally uniform spectrum of waves from the troposphere. For this study, wind components are retrieved on the native 137 model levels. To prepare the data for analysis, the geopotential height of each model level is first converted to geometric altitude. The vertical profiles are then linearly interpolated from this native geometric altitude grid onto the standard 100 m high-resolution grid used for all datasets in this study, and then interpolated to our high resolution analysis grid using geopotential height, temperature, and humidity.

98

99

100

101 102

103

104

105

107

108 109

110

111

112

113 The GNSS-RO method offers many advantages for studying atmospheric dynamics, particularly GW activity and parameters. 114 The first RO-derived GW estimates date back from the early 2000s and several missions have since provided data for further 115 studies, focusing on potential energy as a proxy for retrieving GW activity (Tsuda et al., 2000; Fröhlich et al., 2007; Wang and 116 Alexander, 2010; Luna et al., 2013; Schmidt et al., 2016). The Radio Occultation Meteorology Satellite Application Facility 117 (ROMSAF) provides global GNSS-RO datasets. For the study period of June 2019 to August 2022 these datasets are dominated 118 by the Metop constellation: Metop-B and Metop-C throughout, with Metop-A contributing until its retirement in November 119 2021 (von Engeln et al., 2011). These datasets are derived from the bending angles of GNSS signals as they pass through the 120 Earth's atmosphere and are observed by low Earth-orbiting satellites. It provides global coverage with a high vertical resolution, 121 sub-Kelvin accuracy, full diurnal coverage, and all-weather capability. The vertical resolution of GNSS-RO temperature 122 profiles is fundamentally limited by diffraction and varies with altitude, typically ranging from ~0.5 km in the lower 123 troposphere to ~1.4 km in the middle atmosphere (Kursinski et al., 1997). While sharp vertical gradients in refractivity (e.g., 124 due to temperature inversions or strong humidity gradients) can be detected, the effective resolution for resolving distinct 125 atmospheric layers is constrained by these diffraction limits. The along-track horizontal resolution is typically around 200-300 126 km. Marquart and Healy (2005) showed that small-scale fluctuations in dry temperature RO profiles could be attributed to 127 GWs with vertical wavelengths equal to or greater than 2 kilometers. Alexander et al. (2008b) suggested analyzing data below 128 30 kilometers in altitude to maintain the signal-to-noise ratio for temperature fluctuations above the detection threshold, which 129 also happens to be Aeolus' maximal capability. Most GW parameters can be derived from single RO temperature profiles. 130 However, estimating momentum flux requires knowledge of the horizontal wave number or wavelength, which cannot be

- 131 deduced from a single temperature profile. To determine the horizontal structure of GWs, it is necessary to analyze clusters of
- 132 three or more profiles adjacent in space and time (Schmidt et al., 2016).
- 134 This study specifically utilizes Aeolus Level 2B Rayleigh clear HLOS winds, ERA5 wind components, and GNSS-RO
- 135 temperature profiles, all brought to a standard interpolated grid to facilitate the accurate comparison and integration of data
- 136 from the different sources. The chosen grid has a vertical resolution of 100 meters and spans a range from 0 to 30 km altitude.
- 137 This approach preserves the maximum vertical detail from each dataset before analysis.
- 139 The choice to compare Aeolus measurements with the ERA5 reanalysis, which does not assimilate Aeolus winds serves as a
- 140 comparison with an independent dataset. This approach thereby highlights, is intentional. This approach allows for a direct
- 141 assessment of Acolus's potential contribution by treating it as an independent dataset, thereby highlighting regions where its
- 142 direct wind measurements might fill observational gaps present in the conventional observing system assimilated by ERA5.

#### 144 2.2 Methods and Limitations

133

138

- 145 The following section discusses the retrieval of GW kinetic energy, Ek. A primary challenge in this retrieval, particularly in
- 146 the tropical UTLS, is the robust separation of GWs from other dominant, synoptic-to-planetary scale equatorial waves, such
- 147 as Kelvin waves. Observational studies using GNSS-RO data have consistently shown that Kelvin waves, with typical vertical
- 148 wavelengths in the range of ~4-8 km (Randel et al., 2021; Randel and Wu, 2005), are a prominent feature of the tropical
- 149 temperature and wind fields. This presents a potential for spectral overlap with the longer vertical wavelength portion of the
- 150 GW spectrum that this study aims to capture.
- 151 Several methods exist for background state determination and large-scale process separation. These broadly fall into two
- 152 categories: Vertical Detrending (VD), often applied to single profiles from instruments like lidars and radiosondes (Gubenko
- 153 et al., 2012; Khaykin et al., 2015), and Horizontal Detrending (HD). HD requires spatially resolved datasets like satellite
- 154 observations or model reanalyses and typically involves spatio-temporal averaging to define the background (Alexander et al.,
- 155 2008b; Khaykin et al., 2015). A comparative study by John and Kumar., (2013) highlighted significant discrepancies in derived
- 156 Ep magnitudes depending on the chosen method.
- 157 The choice of detrending method is particularly critical in the tropics due to the presence of waves like Kelvin waves. VD
- 158 methods, if not carefully designed, may inadvertently remove GWs with long vertical wavelengths or, conversely, retain short
- 159 vertical wavelength components of planetary-scale waves (e.g., Kelvin waves observed with vertical wavelengths as short as
- 160 3 km, as noted by Alexander and Ortland., (2010) and Cao et al., (2022)). Consequently, Schmidt et al. (2016) strongly
- 161 recommend using HD for satellite data, as VD may overestimate GW activity by including remnant signals from synoptic and
- 162 planetary waves that possess significant vertical structure in the tropics. Given these considerations, our study employs an HD

approach, calculating the background profile within a fixed spatio-temporal grid (20° longitude × 5° latitude over 7 days), which we deem best suited for retrieving GW energy information from the Aeolus, GNSS-RO, and ERA5 datasets.

The separation of the wind or temperature profile into a background state and perturbations using HD is intended to isolate 165 fluctuations characteristic of gravity waves by filtering out larger-scale and slower-evolving processes like the mean 166 components of Rossby and Kelvin waves. This selection relies on the distinct scale and structural characteristics of GW 167 168 perturbations. However, the work by Randel et al., (2021) using dense COSMIC-2 RO data reveals further complexities. They 169 found that "residual" small-scale temperature variances (analogous to our perturbation fields) exhibit coherent maxima in the 170 longitudinal and vertical shear zones of large-scale Kelvin waves. This suggests that the local atmospheric environment shaped 171 by Kelvin waves, particularly variations in static stability (N2), can modulate the amplitude of smaller-scale variability, 172 potentially including GWs. Furthermore, data assimilation studies have demonstrated that the inclusion of Aeolus wind data 173 directly impacts the representation of vertically propagating Kelvin waves in numerical weather prediction models. This 174 impact is explicitly linked to the background wind, with the largest analysis changes occurring in regions of strong vertical 175 wind shear (Žagar et al., 2021, 2025). This highlights the importance of direct wind observations in these critical 176 regions. Indeed, direct analysis of Aeolus observations (without assimilation) confirms that Kelvin waves are well-resolved, 177 showing good agreement in wave variances when compared to reanalyses (Ern et al., 2023). This implies that the 178 characteristics of Kelvin waves seen by Aeolus are robust and may differ from those in reanalyses not assimilating Aeolus 179 data\_Furthermore, the assimilation of Aeolus wind data itself has been shown to directly impact the representation of vertically 180 propagating Kelvin waves in numerical weather prediction models, especially in regions of strong vertical wind shear (Žagar 181 et al., 2021). This implies that Kelvin waves are indeed present in the Aeolus observations and that their characteristics might

Mis en forme : Anglais (Royaume-Uni)

combined with a vertical band-pass filter applied to the perturbation profiles. This filter targets vertical wavelengths between
1.5 km and 9 km. The lower limit is chosen based on the effective vertical resolution of the instruments (particularly Aeolus),
while the upper limit of 9 km is selected to be slightly above the typical dominant vertical wavelengths reported for Kelvin
waves in the UTLS, thereby further reducing their potential contribution. This combined HD and vertical filtering methodology
has been widely used for retrieving GW Ep from temperature data (Alexander et al., 2008b; Schmidt et al., 2008; Šácha et al.,
2014; Khaykin et al., 2015), and the availability of Aeolus wind profiles allows us to apply a consistent approach for GW Ek.

To further refine the isolation of GWs and address the potential aliasing from such equatorial waves, our HD approach is

Nevertheless, it is acknowledged that a perfect separation is difficult. The sharpest vertical gradients associated with Kelvin waves, or localized enhancements of GW activity within Kelvin wave-modified environments as suggested by Randel et al., (2021) might still contribute to the derived GW energy. The interpretation of our GW Ek and Ep must therefore consider this

193 context, particularly when analyzing variability in regions known for strong equatorial wave activity.

differ from those in reanalyses not assimilating Aeolus data.

182

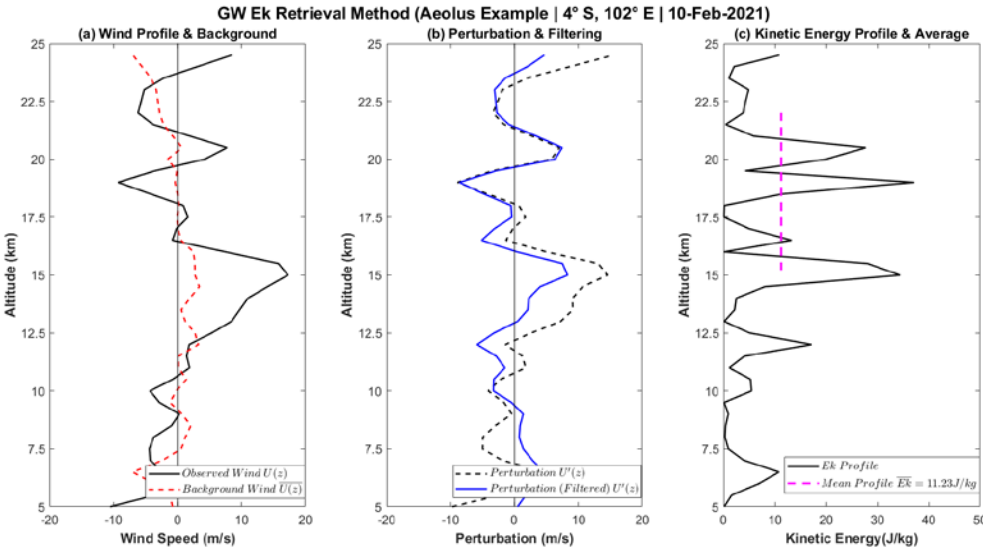


Figure 1. Derivation of GW energy profiles from wind measurements (a) Observed wind profile and the corresponding background state profile. (b) Wind perturbation profile alongside its filtered counterpart. (c) Resulting in Ek, smoothed and then averaged within the given altitude range.

Based on the linear theory of GW, the measured wind profile U(z) shown in Fig.1a is divided into a background wind  $\overline{U}(z)$  also present in Fig.1a and a perturbation U'(z) depicted in Fig.1b. The background is obtained by averaging all individual wind profiles for kinetic energy retrieval, within a spatiotemporal grid box of 20° longitude  $\times$  5° latitude over 7 days. While this horizontal detrending method was originally demonstrated using temperature profiles in Alexander et al., (2008b), its application to wind profiles is theoretically sound. Linear gravity wave theory dictates that wind and temperature perturbations are coupled manifestations of the same wave phenomena, and thus the principle of separating smaller-scale waves from the large-scale background flow via spatiotemporal averaging is equally valid for both fields. Following the arguments presented in Alexander et al., (2008b), this choice is justified by the need to ensure a sufficient number of profiles per grid cell, which minimizes random noise while preserving meaningful variability in the data. Shorter temporal windows would lead to insufficient sampling, while longer windows would smooth out critical small-scale wave features. The grid size is also designed to preserve the spatiotemporal variability of mesoscale gravity waves and equatorially trapped structures, in an attempt to separate the background and perturbation components without introducing significant biases.

211 Finally, this configuration mitigates errors in the definition of the  $\overline{U}(z)$  profile, ensuring reliable kinetic energy calculations 212 and robust separation of gravity wave perturbations. We performed sensitivity tests with varying grid sizes and temporal 213 windows to confirm that this configuration provides the best possible background state when prioritizing Aeolus retrieval (see 214 Fig. A1 in Appendix A). The average number of profiles used for the background state determination is 55 for Aeolus, 20 for GNSS-RO and 1400 for ERA5. 215

216

217 The next step involves subtracting the background profile from its corresponding individual profile, eliminating most large-218 scale waves (Planetary Waves, Kelvin Waves, Rossby Waves). This yields the perturbation profile U'(z), which is then 219 subjected to Welch-windowing, which is done in order to mitigate spectral leakage (Alexander et al., 2008a; 2008b; Khaykin 220 et al., 2015). A prior study also applied a similar windowing function (half cosine), aiming to counteract the "effects of the 221 edge of the height range" (Hei et al., 2008). After said windowing, a band-pass filter designed to retain vertical wavelengths 222 between 1.5 km and 9 km. is applied to the perturbation profile, as seen in Fig.1b and 1c. The upper limit of 9 km isolates 223 GWs from larger-scale planetary waves, consistent with our background removal strategy. The lower limit of 1.5 km is chosen 224 to reflect the effective vertical resolution of the Aeolus instrument (Ratynski et al., 2023) and ensures that our comparison is 225 restricted to wave scales reliably resolved by all datasets (Banyard et al., 2021). This procedure provides a methodologically 226 consistent basis for comparing GW energy across the different instruments.

227

229

The GW Ek can be derived from the variance of wind components as follows: 228

230 
$$E_k = \frac{1}{2} \left( \overline{u'^2} + \overline{v'^2} + \overline{w'^2} \right),$$
 (2)

231

232 where u, v, and w represent the zonal, meridional, and vertical wind components, respectively. Considering that Aeolus's viewing geometry in the tropics makes its HLOS wind primarily sensitive to the zonal component (as shown in Eq. 1), we will 233 234 note all mentions of retrieved speed as u for clarity. In our case, since the vertical wind speed is neglected and the satellite is 235 not able to distinguish between zonal and meridional wind, it is necessary to provide a new formalism for the retrieved metric:

$$236 \quad E_{k \, HLOS} = \frac{1}{2} \left( \overline{u'^2}_{HLOS} \right) \tag{3}$$

238

237

The resulting profile, which is essentially the perturbation squared, is cut to keep the data between one kilometer below the 239 tropopause and 22 km. The altitude range is chosen considering Aeolus' limitations, such as increasing error at higher altitudes 240 due to lack of backscatter signal (Ratynski et al., 2023, their Fig.3). The lower bound is set one kilometer below the tropopause 241 to focus on events extending beyond it, balancing Aeolus' resolution with our interest in upper end dynamics. For consistency, 242 the tropopause height is derived directly from the ERA5 dataset for all analyses. The tropopause is calculated for each profile based on the WMO thermal definition, where the tropopause is the lowest level at which the lapse rate decreases to 2 K/km or

less, provided the average lapse rate within the 2 km layer above remains below this threshold. The profile is then averaged over the selected range, representing the Ek, as seen in Fig.1c.

246 We acknowledge that including the layer just below the tropopause presents a potential challenge, as strong, non-wave 247 divergent outflow from deep convection could be partially aliased into our derived kinetic energy (Stephan et al., 2021). To 248 rigorously test the robustness of our results against this potential contamination, we have performed a comprehensive 249 sensitivity analysis by recalculating the kinetic energy fields using two more conservative averaging layers, starting from 1 250 km and 2 km above the tropopause, respectively (see Fig.B1 and B2 in Appendix B). By shifting the analysis layer upward to 251 such levels, we confirm that the geographical patterns of the energy hotspots are remarkably stable (spatial correlation r > 252 0.83), and that the vast majority of the peak energy (~88-91%) persists well into the stratosphere. If the signal were dominated 253 by shallow tropospheric outflow, the energy peaks would have collapsed when the analysis layer was moved above the 254 tropopause. The fact that a strong, structured signal remains confirms that our method is observing vertically propagating 255 gravity waves that have penetrated the lower stratosphere. The detailed results of this analysis confirm that our main conclusions are not sensitive to this choice.

256 conclusions are not sensitive to this choice257

265

271

Although the above steps focus on retrieving GW Ek from Aeolus wind measurements, the same procedure can be applied to temperature-based observations such as GNSS-RO for Ep. The main difference lies in substituting temperature T(z) for wind U(z) throughout the background-perturbation decomposition, which means using T'(z) rather than U'(z). The Welch window was applied to all perturbation profiles (wind and temperature) before filtering to mitigate spectral leakage. The same band-pass filtering strategy and vertical averaging then provide the Ep profile from the temperature perturbations. In this case, the GW Ep is calculated using this formula:

$$264 E_p = \frac{1}{2} \left(\frac{g}{N}\right)^2 \left(\frac{T'}{\bar{\tau}}\right)^2$$
(4)

The  $E_{k\,HLOS}$  metric derived from Aeolus (Eq. 3) represents the kinetic energy projected onto the instrument's line of sight. Since our study focuses on the tropical UTLS region, the meridional wind component will have a minor contribution compared to the zonal component. Therefore, the  $E_{k\,HLOS}$  energy represents primarily the zonal activity, meaning that we are missing a non-negligible proportion of wave activity. To evaluate the contribution of v' to the total kinetic energy we use ERA5 data and compute the ratio between total Ek (derived from u' and v') and  $E_{k\,HLOS}$  (as it is observed by ALADIN).

This ratio (Fig. C1 in Appendix C1) exhibits significant geographic variability, which can be linked to physical mechanisms that create wave anisotropy. For instance, over regions like the Indian Ocean, the ratio is relatively low (~1.5), suggesting a predominantly zonal orientation of wave energy. This is physically plausible, as persistent surface winds like the trade winds can influence the tropopause-level wave field through two main processes. Firstly, flow over orography can preferentially

276 generate zonally-oriented waves (Kruse et al., 2023). Secondly, the background wind profile itself acts as a directional filter, 277 selectively allowing waves propagating in certain directions to reach the UTLS while attenuating others through critical-level 278 interactions (Plougonven et al., 2017; Achatz et al., 2024).

279

286 287

288

289

290291

292

293

294

304

280 When averaged over the mission period and focused on the equatorial band ( $10^{\circ}\text{S}-10^{\circ}\text{N}$ ), the ratio settles at approximately 1.6. This implies that  $Ek_{HLOS}$  accounts for around 62.5% of total Ek, the remainder being undetectable due to HLOS 282 projection. The meridional component, less significant in this specific geographical area for Aeolus, contributes the remaining 283 37.5% of Ek not considered by  $Ek_{HLOS}$ . Although not dominant,  $Ek_{HLOS}$  represent a substantial contribution to Ek. This 284 scaling factor is used when discussing the implications of our Aeolus findings for the total GW kinetic energy budget. The details of the spatio-temporal variability of this ratio are provided in the Appendix C.

The methods employed constrain the analysis to a specific range of horizontal and vertical wavelengths. Aeolus' RBS determines the spacing between sampling points, impacting the vertical and horizontal resolution and maximal detectable wavelength. The vertical wavelength analysis is constrained by the 9 km upper band-pass, representing roughly half the average profile length in the tropics, after limiting the profile to the optimal range and especially considering the dynamic lower bound. Profiles generally extend to heights between 23km and 26km. In the horizontal dimension, since a 20° x 5° degrees grid is used for the background removal and the wind is supposed quasi-zonal, the zonal wavelengths, therefore, reside below 2220 km.

295 Additionally, Aeolus can be prone to errors alternating the quality of wind profiles. Amongst the most notable ones are dark 296 currents in the charge-coupled devices ("hot pixels"), potentially leading to errors of up to several meters per second (Weiler 297 et al., 2021). Another identified issue is the oscillating perturbations, parasitic deformations of the signal, yet to be attributed to a cause, which can be mistaken for GW-induced signals (Ratynski et al., 2023). While corrections were implemented for 298 299 the first issue (Weiler et al., 2021), the overall signal random error varies with time, with a general tendency to increase due 300 to instrument degradation (Lux et al., 2022). Aeolus' HLOS wind variance is inherently linked to the measurement noise (i.e., 301 random error). In other words, the observed wind variance is a sum of the variance due to waves (detected using the given data 302 and method) and the variance due to ALADIN noise, i.e., its random error squared.

$$303 \quad \overline{u'^{2}_{HLOS}} = \overline{u'^{2}_{GW}} + \overline{u'^{2}_{I.N}} \tag{5}$$

with  $\overline{u'^2}_{GW}$  representing the variance contribution from gravity waves and  $\overline{u'^2}_{LN}$  the contribution from instrument noise. Since kinetic energy is proportional to variance, this relationship holds for kinetic energy as well. The observed Aeolus kinetic energy  $\overline{Ek_{Aeolus\,HLOS}}$  is therefore the sum of the true geophysical signal and a noise component which increases over the mission lifetime. To isolate the true gravity wave energy, this time-varying noise component must be estimated and removed. This

309 correction is performed at the kinetic energy level. While radiosondes provide a valuable independent reference, their sparse

310 coverage in the tropics makes them unsuitable for creating a globally consistent correction field. We therefore use the ERA5

311 reanalysis as a temporally stable global reference to estimate the Aeolus instrument noise. The core principle is to produce a

312 corrected dataset, denoted as  $\overline{Ek_{Aeolus\,HLOS*}}$  by subtracting our best estimate of the noise energy  $\overline{Ek_{I.N}}$  from the observed

313 energy

$$314 \quad \overline{Ek_{Aeolus\,HLOS^*}} = \overline{Ek_{Aeolus\,HLOS}} - \overline{Ek_{I.N}}$$
 (6)

315 The estimation of the noise term,  $\overline{Ek_{LN}}$ , is not a simple subtraction. It is derived using a spatio-temporally adaptive algorithm

316 that blends an additive offset (representing baseline instrument noise, dominant in quiescent atmospheric regions) with a

317 multiplicative scaling factor (more influential in active convective regions where noise effects might scale with the signal).

318 This adaptive approach ensures that instrumental artefacts are removed without suppressing the high-energy gravity wave

319 hotspots uniquely captured by Aeolus, or over-correcting areas of low variance.

320 An additional refinement step is required for seasonally averaged geographical maps. To produce these maps, individual profile

321 energy values were first binned into a  $5^{\circ}$  longitude by  $2^{\circ}$  latitude grid. A second stage adapts the noise correction derived from

322 the tropical 10°S-10°N band for application to the broader latitudinal extent of the maps (e.g., 30°S-30°N), accounting for

323 latitudinal variations in energy and ensuring physically consistent, non-negative results. To reduce noise and highlight large-

324 scale patterns, a 3-point median filter followed by a 3-point moving average filter was applied sequentially in both the zonal

325 and meridional directions.

326 The full mathematical derivation of the adaptive estimation of  $\overline{E}k_{l,N}$ , the details of the map-specific refinement, and a series

327 of diagnostic plots, including comparisons of Aeolus data before and after correction to validate the assumptions made, are

328 provided in the Appendix D.

### **3. Results**

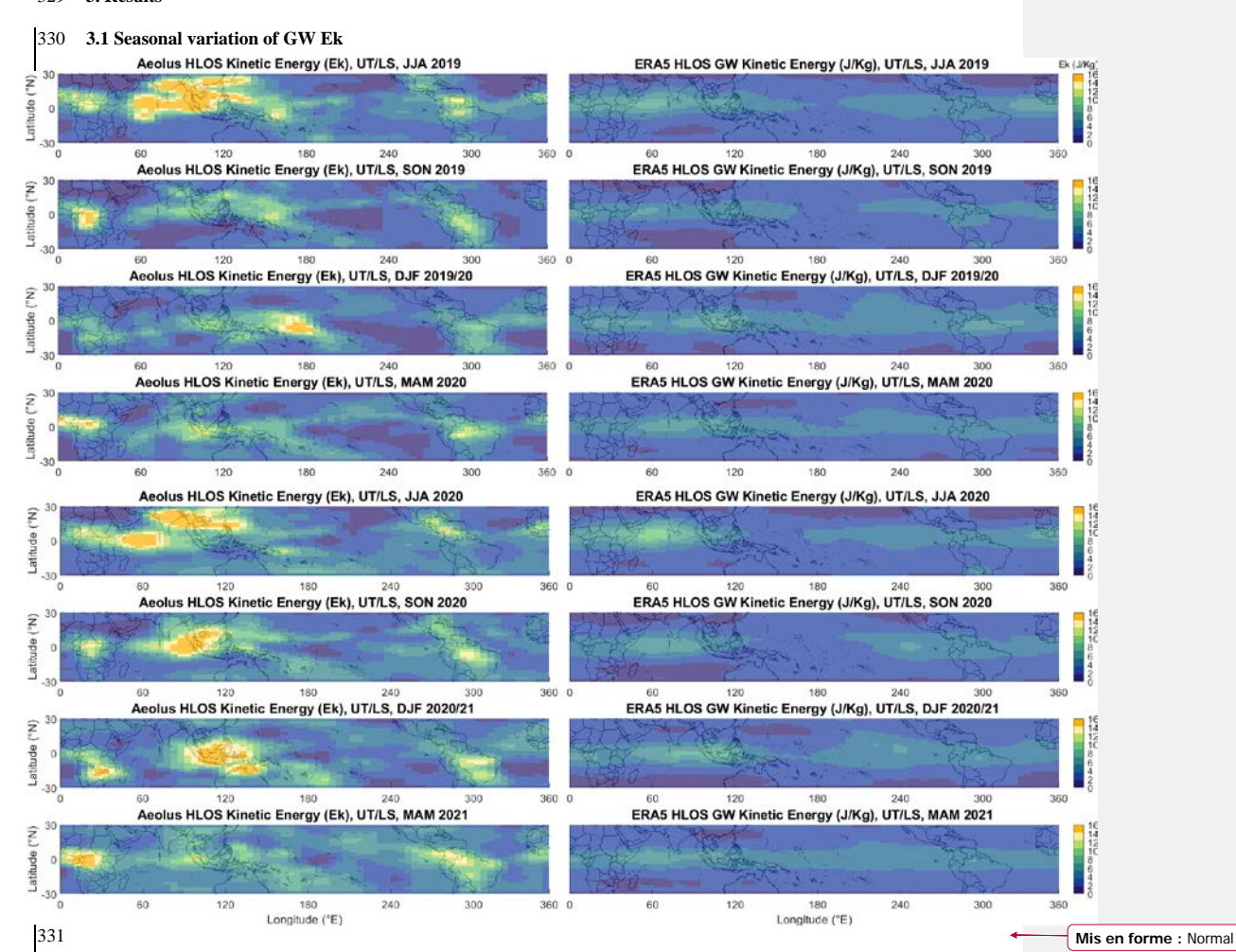


Figure 2. Comparison between  $Ek_{Aeolus\,HLOS}$ , (left column) and  $Ek_{ERA5\,HLOS}$  (right column). Each line row corresponds to a season, from June-July-August 2019 to March-April-May 2021. The UTLS altitudes are defined between one kilometer below the tropopause and 22 km. The tropopause is determined from the ERA5 reanalysis. The maps are smoothed using a combination of median and moving average filters as described in the Methods section.

337 2020, derived from the corrected Aeolus observations and the ERA5 reanalysis. This comparison reveals both key similarities 338 in two large-scale patterns: first, the confinement of most GW kinetic energy to the equatorial belt (approximately 15°S-15°N), 339 and second, a distinct seasonal migration of this energy. However, there are also significant differences in the representation of regional wave activity. This comparison reveals both key similarities in large scale patterns and significant differences in 340 341 the representation of regional wave activity. 342 Both datasets consistently show that the majority of GW kinetic energy is confined to the equatorial belt (approximately 15°S– 343 15°N). This observation aligns with the expectation that deep tropical convection, concentrated within the Intertropical 344 Convergence Zone (ITCZ), is a primary source of the observed waves. The reader should note that some variance from other 345 equatorial waves, centered at the equator by definition, will also be inevitably present to a small degree in the perturbation 346 fields. A clear seasonal cycle is evident in both Aeolus and ERA5. During Boreal summer (JJA), enhanced Ek is prominent over Central Africa and the Indian Ocean. This corresponds to the active phases of the African and Indian monsoon systems, 347 348 which provide a persistent, large-scale environment favorable for the development of organized, deep convective systems 349 known to be efficient gravity wave generators (Forbes et al., 2022). During Boreal winter (DJF), the focus of activity shifts eastward towards the Maritime Continent and the Western Pacific, coinciding with that region's primary convective season. 350 351 These general patterns are also consistent with previous climatologies of GW potential energy derived from temperature

Figure 2 displays the Ek<sub>HLOS</sub> distribution from <u>JJA 2019 to MAM 2021</u>the Boreal Spring of 2019 to the Austral summer of

336

352

353

354

355 356

357

358

359

360

361 362

363

364

365

aligned with our observations.

It is also necessary to clarify the interpretation of the wave activity observed at the subtropical edges of our analysis domain (near 30°N/S). While our study focuses on convectively generated waves originating from the deep tropics, the kinetic energy measured in the subtropics is likely dominated by different, local sources. The strong subtropical jets and associated frontal systems are potent generators of inertia-gravity waves through mechanisms of geostrophic adjustment and shear instability (Kruse et al., 2023; Plougonven and Zhang, 2014). A recent case study has confirmed that such jet-merging events can produce significant, large-scale GW fields (Woiwode et al., 2023). These jet- and front-generated waves typically have sub-weekly periods and significant wind perturbations, meaning they fall within the detection window of our filtering methodology (Achatz et al., 2024). Therefore, the enhanced energy often visible near 30°N and 30°S in our seasonal maps should be interpreted as stemming primarily from these midlatitude dynamical processes, rather than from the poleward propagation of the equatorial convective waves.

measurements Alexander et al. (2008b, their Fig.3 and Fig.4). The GNSS-RO derived Ep values, which range from 0 to 6.6

J/kg at 15 km and 0 to 4.4 J/kg at 22 km (Alexander et al., 2008c), after applying the usual Ek/Ep ratio of 1.6, are generally

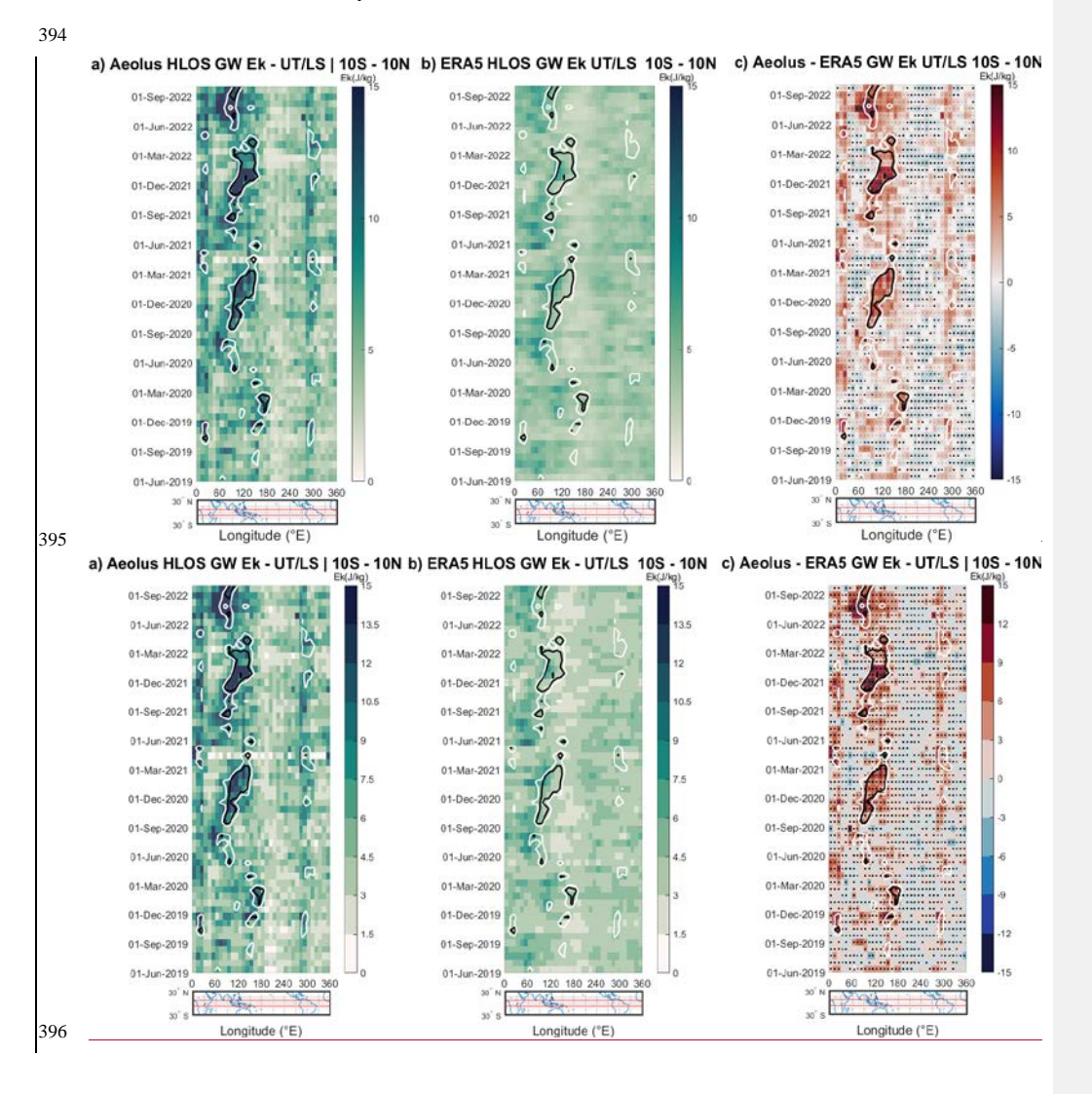
Despite these general agreements, a critical difference emerges in the structure and intensity of the energy hotspots. <u>ERA5</u> tends to represent GW activity as a relatively smooth, zonally elongated band, with modest seasonal modulation and appears

369 equator ERA5 tends to represent GW activity as a relatively smooth, zonally elongated band, with modest seasonal modulation. 370 In stark contrast, Aeolus reveals a picture of much more localized and intense Ek hotspots. For example, during JJA 2020 and 371 SON 2020, Aeolus observes a well-defined hotspot over the Indian Ocean with Ek values exceeding 10-12 J/kg, whereas 372 ERA5 shows only a diffuse enhancement in the same region with values rarely exceeding 5-7 J/kg. Similarly, the DJF 2020/21 373 hotspot over the Maritime Continent is markedly stronger and more geographically confined in the Aeolus data. 374 This discrepancy suggests that while ERA5 captures the broad climatic envelope of convective GW activity, it significantly 375 underestimates the peak energy of waves generated by localized, intense convective systems. This is particularly evident in regions where conventional wind observations are sparse, such as the Indian Ocean. The direct wind profiles from Aeolus 376 377 appear to capture magnitudes and structures of this convection-driven wave activity that are not present in the reanalysis. The period from mid-2020 onward, which coincided with the development of La Niña conditions, exhibits the most 378 379 pronounced differences between the two datasets. While La Niña is known to enhance convection over the Maritime Continent, 380 the consistently higher energy levels observed by Aeolus across all regions during this period also correlate with a documented increase in the satellite's instrumental random error (Ratynski et al., 2023, their Fig.6). Our adaptive noise correction (see 381 382 Appendix D) is designed to account for this degradation. However, it is challenging to perfectly disentangle the increased 383 geophysical signal (e.g., from La Niña) from the effects of increased instrument noise. Nevertheless, the geographical consistency of the hotspots observed by Aeolus, which align with known convective centers, provides confidence that the 384 385 primary patterns represent true atmospheric phenomena that are underrepresented in the reanalysis. The direct link between 386 these kinetic energy hotspots and deep convection will be examined in detail in the following section through a comparison 387 with Outgoing Longwave Radiation data. Finally, regarding the strong latitudinal confinement of the signal, while this is primarily a physical feature, our noise-388 389 correction methodology may also contribute to it. As detailed in the Appendix D (Part 2), the correction is weighted by the latitudinal structure of the raw signal. This approach, designed to avoid over-correction in low-signal subtropical regions, 390 naturally sharpens the latitudinal gradient at the edges of the tropical belt. 391

to significantly miss wave activity both in the active monsoon regions and in more structured events further from the

368

# 3.2 Zonal variation of GW activity from observations and ERA5



399 of over 3 weeks and 10 degrees. The white bins represent the lack of satellite information in (a). The OLR measurements were obtained from the Australian Bureau of Meteorology. The UTLS altitudes are defined between one kilometer below the tropopause 401 and 22 km. The tropopause is determined from the ERA5 reanalysis. Black stippling indicates regions where the difference between 402 quantities is statistically significant (two-sample t-test, p < 0.05). 403 404 To assess the evolution and transition between the different seasons with greater precision, the Hovmoller diagrams in Fig.3 405 only show the HLOS-projected GW kinetic energy from Aeolus and ERA5, along with their difference within the deep tropics 406 between 10° N and 10° S, as Fig.2 proves this region contains most of the activity. To identify regions of deep convection, these diagrams are overlaid with contours of low Outgoing Longwave Radiation (OLR), a reliable proxy for deep convection 407 408 as it indicates cold, high-altitude cloud tops and thus the depth of convective systems (Zhang et al., 2017). 409 Fig.3a shows Ek<sub>Aeolus HLOS\*\*</sub>, where prominent hotspots of high Ek (often attaining 15 J/kg) are visible, with a broad region of 410 411 enhanced activity migrating eastward from the African continent (~0-60°E) towards the Indian Ocean and Maritime Continent 412 (~60-150°E) between June and March. This shift is recurring over multiple years and shows a relative consistency between 413 each year in terms of longitudinal and temporal range. This migration of high Ek is systematically co-located with the seasonal 414 cycle of convection, with the hotspots consistently falling within the low OLR contours (below 220 W/m²). 415 To assess the evolution and transition between the different seasons with greater precision, the Hovmoller diagrams in Fig.3 416 only show the observations within the deep tropics between 10° N and 10° S, as Fig.2 proves this region contains most of the 417 activity. Fig.3a shows Ekacolus HLUSS; where prominent hotspots of high Ek (often attaining 15 J/kg) are visible, with a broad 418 region of enhanced activity migrating eastward from the African continent (~0-60°E) towards the Indian Ocean and Maritime 419 Continent (~60 150°E) between June and March. This shift is recurring over multiple years and shows a relative consistency 420 between each year in terms of longitudinal and temporal range. 421 422 The presence of hotspots, represented by distinct shapes in the Ek patterns, is expected in regions with prevalent convective 423 activity. These can be attributed to multiple powerful wave generation mechanisms occurring at the scale of individual storms. 424 One primary mechanism is thermal forcing, where the pulsatile nature of latent heat release in a convective updraft acts like a 425 piston on the surrounding stable air, generating a broad spectrum of gravity waves (Beres et al., 2005). A second, 426 complementary mechanism is mechanical forcing, where the body of the strong updraft itself acts as a physical barrier to the 427 background wind. The flow forced over this "moving mountain" generates large-amplitude, low-phase-speed waves that are 428 stationary relative to the storm (Corcos et al., 2025; Wright et al., 2023). The strong spatial correlation shown in Figure 3a 429 between the most intense kinetic energy observed by Aeolus and the lowest OLR values (< 210 W/m²) provides evidence that 430 these mechanisms are the primary drivers of the observed GWs. The intense kinetic energy observed by Aeolus is likely the

Figure 3. (a,b,c) Hoymoller diagram of Ek<sub>Aeolus HLOS</sub>, Ek<sub>ERAS HLOS</sub> and their difference. The contour plot represents the Outgoing Longrange Longwave Radiation (OLR) for 210 and 220 W/m<sup>2</sup> (black and white, respectively). Each bin corresponds to an average

398

signature of both mechanisms operating within active convective systems. These convectively generated GWs can propagate

- 432 vertically and interact with the large-scale atmospheric circulation, transferring momentum and energy to the background flow
- 433 (Alexander et al., 2021).
- 434 In sharp contrast, Fig.3b presents a much more subdued and less dynamic picture for the corresponding ERA5 perspective.
- 435 While ERA5 shows some broad, low-amplitude enhancement of Ek that co-locates weakly with the seasonal convective cycle,
- 436 it completely fails to capture the intense, high-energy hotspots observed by Aeolus. The organized eastward propagation and
- 437 the high peak energy values are entirely absent in the reanalysis. For nearly all regions and time periods, the Ek in ERA5
- 438 remains below 7 J/kg.
- 439 The difference between the two datasets, shown in Fig.3c, quantifies this discrepancy. The plot is overwhelmingly positive,
- 440 indicating a systematic and significant underestimation of GW kinetic energy by ERA5 throughout the tropics. The regions of
- 441 greatest underestimation, where the difference exceeds 10 J/kg, align almost perfectly with areas of deep convection, as
- 442 identified by the low OLR contours. This last element reinforces the conclusion that ERA5's key limitation lies in its
- 443 representation of convection-driven wave activity. This finding is consistent with the fact that ERA5's non-orographic GWD
- 444 scheme is not directly coupled to model-diagnosed convection, highlighting the need for improved parameterizations to better
- 445 <u>capture these sources.</u>
- 446 The difference between the two datasets, shown in Fig.3c, quantifies this discrepancy. The plot is overwhelmingly positive,
- 447 indicating a systematic and significant underestimation of GW kinetic energy by ERA5 throughout the tropics. The regions of
- 448 greatest underestimation, where the difference exceeds 10 J/kg, align almost perfectly with areas of deep convection, as
- 449 identified by the low Outgoing Longwave Radiation (OLR) contours. The OLR represents the amount of terrestrial radiation
- 450 released into space and, by extension, the amount of cloud cover and water vapor that intercepts that radiation in the
- 451 atmosphere. It is a widely used and reliable proxy for deep convection due to its strong correlation with diabatic heating (Zhang
- 452 et al., 2017), reinforcing the conclusion that ERA5's primary weakness lies in representing convection driven wave activity.
- 453 To confirm the robustness of this finding, a two-sample t-test was performed for each grid cell. The stippling in Fig.3c indicates
- 454 where the mean Ek from Aeolus is statistically significantly higher than that of ERA5 (p < 0.05). The pervasive stippling
- 455 across nearly all convective hotspots underscores that the observed differences are not random fluctuations but represent a
- 456 fundamental deficiency in the reanalysis. This finding suggests that without the assimilation of direct, high-resolution wind
- 457 profile data like that from Aeolus, reanalysis models may not fully resolve the kinetic energy associated with gravity waves
- 458 generated by localized, intense convective events. An alternative display of Fig.3c as a ratio, along with an F-test, can be found
- 459 in Appendix E.

# 4. Comparison with Potential Energy: possibilities and limitations

461

471

472

While a conservative analysis might prioritize directly comparable metrics, exploring less conventional approaches can reveal patterns that remain hidden in traditional frameworks. A key goal of this study is to compare the kinetic energy from Aeolus with potential energy, the most common metric for GW climatologies. However, this comparison is complicated by the longstanding assumption of a constant Ek/Ep ratio.

Traditionally, linear gravity wave theory proposes a near-constant ratio of Ek to Ep, often quoted between 5/3 and 2.0 (Hei et al., 2008; VanZandt, 1985). In stable, linear wave conditions, these theoretical predictions hold reasonably well (Nastrom et al., 2000). However, a growing body of evidence from empirical studies reveals significant variability in this ratio, suggesting that real-world atmospheric conditions often involve non-linear processes such as wave breaking or saturation, which are not accounted for in the linear theory (Baumgarten et al., 2015; Guharay et al., 2010; Tsuda et al., 2004).

Code de champ modifié

Mis en forme : Français (France)

Mis en forme : Français (France)

# ERA5 EK/EP UT/LS 10S-10N 01-Sep-2022 01-Jun-2022 2.8 01-Mar-2022 2.6 01-Dec-2021 2.4 01-Sep-2021 01-Jun-2021 2.2 01-Mar-2021 01-Dec-2020 1.8 01-Sep-2020 01-Jun-2020 1.6 01-Mar-2020 1.4 01-Dec-2019 1.2 01-Sep-2019 01-Jun-2019 60 120 180 240 300 360 0 $30^{\circ} \, N$

Longitude (°E)

30° S



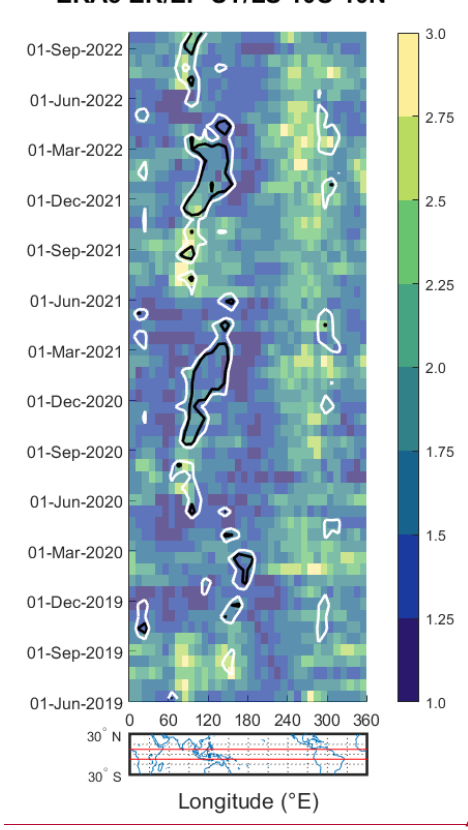


Figure 4. Spatiotemporal distribution of the Ek/Ep ratio in the ERA5 reanalysis for the equatorial band (10°S–10°N). The UTLS altitudes are defined between one kilometer below the tropopause and 22 km. White and black contour lines represent 210 and 220 W/m2 OLR, respectively The contour-plot represents the Outgoing Longrange Radiation (OLR) for 210 and 220 W/m² (black and white, respectively). Each bin corresponds to an average of over 3 weeks and 10 degrees. The OLR measurements were obtained from the Australian Bureau of Meteorology. The tropopause is determined from the ERA5 reanalysis.

To illustrate this complexity within a self-consistent framework, we first examine the Ek/Ep ratio derived entirely from the ERA5 reanalysis. Figure 4 presents the longitudinal and temporal variations of this ratio in the equatorial UTLS. The figure immediately reveals that the ratio is far from constant. It exhibits significant spatial and temporal variability, with values frequently exceeding the linear theory predictions (>2). Notably, distinct hotspots of high Ek/Ep ratios are present, particularly over the Indian Ocean at around 70° and the South American continent at 300°.

487 show a correct correspondence. This suggests that when wave generation is not dominated by deep convection, ERA5 can 488 reproduce realistic GW structures. The strong agreement in these non-convective regions also reinforces the idea that the dominant winds have a strong zonal component, as the quasi-zonal  $u_{HLOS}$  measurement from Aeolus is sufficient to capture 489 490 these features. The elongated white stripe during February-March 2020 comes from an intense intraseasonal disturbance, the 491 2020 Madden-Julian Oscillations (MJO), which can inject unusually strong gravity-wave energy into the upper troposphere 492 (Kumari et al., 2021). 493 The divergence between ERA5 and Aeolus becomes most pronounced precisely in the deep convective regions where Aeolus 494 observes its strongest Ek signals, inside the areas of low OLR. The discrepancy appears specifically linked to convection-495 driven dynamics, which are either not properly represented or fail to trigger sufficient wave activity within the ERA5 model's 496 parameterizations. This suggests that the primary cause of ERA5's underestimation is not a simple mispartitioning between the horizontal wind components (i.e., a directional bias in the line-of-sight projection) but rather a more fundamental, large-497 498 scale underestimation of the total kinetic energy. 499 This model-internal result demonstrates that relying on a fixed ratio to infer one energy component from another is likely to 500 be inaccurate, especially in dynamically convectively active regions. The partitioning of energy between kinetic and potential 501 forms is itself a key diagnostic of wave dynamics that requires further observational constraints. 502 One promising possibility of this study in providing deeper context lies in comparing the kinetic energy of gravity waves observed by Aeolus with the potential energy derived from GNSS-RO data. GNSS-RO provides high-resolution temperature 503 504 profiles that are used to estimate the potential energy of gravity waves. Previous studies that looked into GW climatology all 505 relied on these estimate to base their observations on, as it was the only global instrumentation available (Schmidt et al., 2008; 506 Alexander et al., 2008b; Šácha et al., 2014; Khaykin et al., 2015). Hence, we will adopt this method of comparison as well.

In regions outside of the most intense convective activity, where ERA5 does manage to represent some kinetic energy

enhancement, the agreement with Aeolus is often satisfactory. This is visible in Fig. 3c, where the same areas (120° and 300°)

485

486

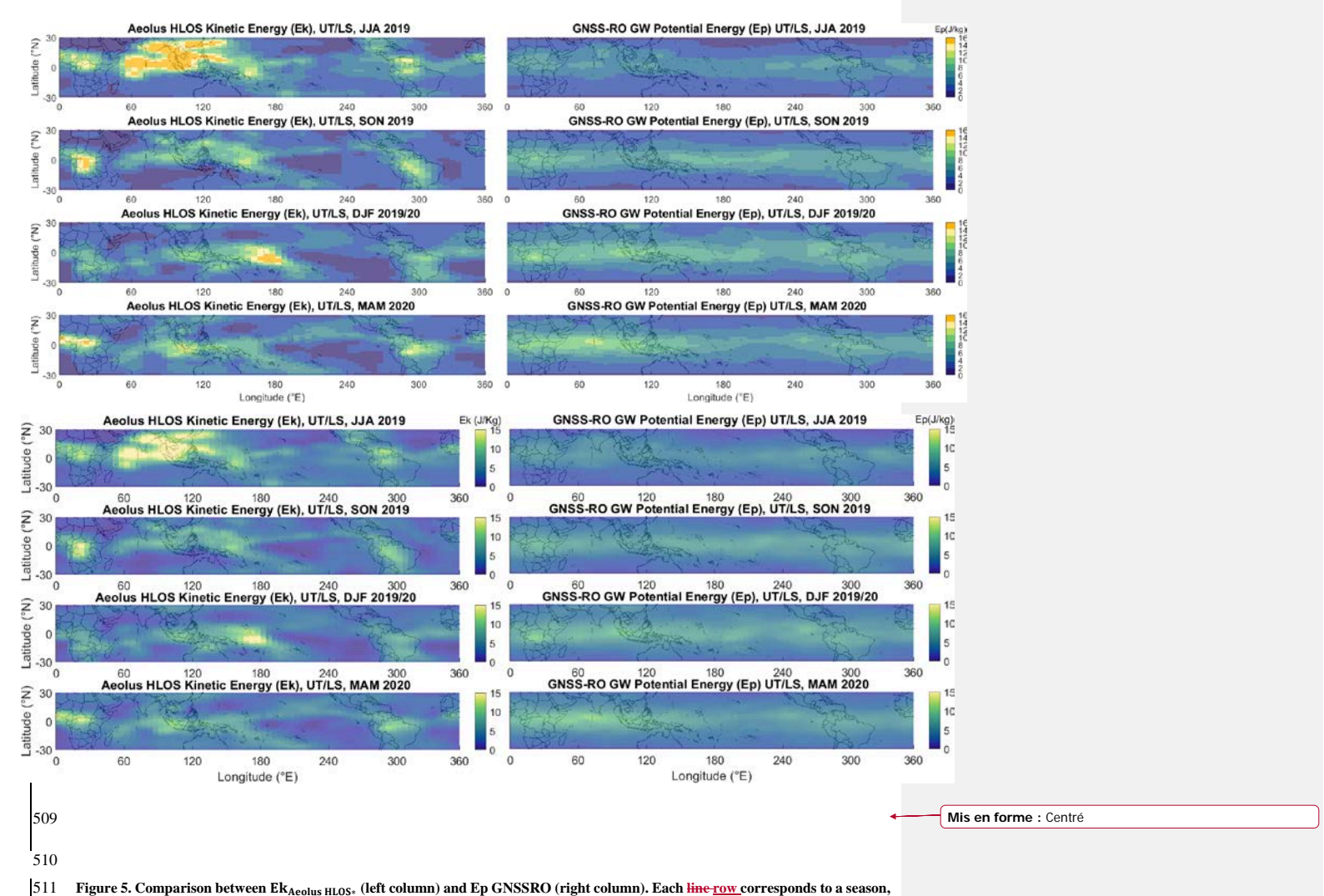


Figure 5. Comparison between Ek<sub>Aeolus HLOS</sub>. (left column) and Ep GNSSRO (right column). Each line row corresponds to a season, from June-July-August 2019 to March-April-May 2020. The white bins represent the lack of satellite information. The UTLS altitudes are defined between one kilometer below the tropopause and 22 km. The tropopause is determined from the ERA5 reanalysis. The maps are smoothed using a combination of median and moving average filters as described in the Methods section.

covering the period from June 2019 to May 2020. The figure highlights key spatial and temporal patterns of gravity wave 516 activity detected by each instrument, with both datasets presenting clear seasonal variability. 517 518 519 Although the ratios between Ek and Ep suggested by linear gravity wave theory generally range between 5/3 and 2.0, empirical observations show significant variability. This variability, which is influenced by geographical factors, nonlinear processes, or 520 521 wave interactions, underscores the importance of examining these two forms of energy from different perspectives rather than 522 seeking strict correspondences. 523 524 With that in mind, what stands out from this comparison is the overall consistency in detecting gravity wave hotspots, particularly within the tropical belt (The African land convection and Indian Ocean hotspot are consistent on both instruments). 525 526 One notable aspect of the comparison is the seasonal shift in gravity wave activity between the two datasets, with both detecting enhanced wave activity during certain months (increased activity levels in DJF and MAM 2020). Because of inherent 527 differences (different line of sight and signal projection, different physical quantities and their varying ratio that is empirically 528 529 challenging the literature, different signal treatment and correction), direct one-to-one comparisons are not appropriate. Nonetheless, it allows us to draw parallels with Aeolus observations, where spatial and temporal correlation of hotspots should 530 531 follow the same disposition, allowing for an independent benchmark. Despite these methodological differences, both instruments align on the seasonal peaks and general distribution of wave activity, reinforcing the reliability of the data. 532

 $Fig. 5 \ offers \ a \ side-by-side \ seasonal \ comparison \ of \ Ek_{Aeolus \ HLOS^*} \ (left \ column) \ and \ Ep \ derived \ from \ GNSS-RO \ (right \ column),$ 

515

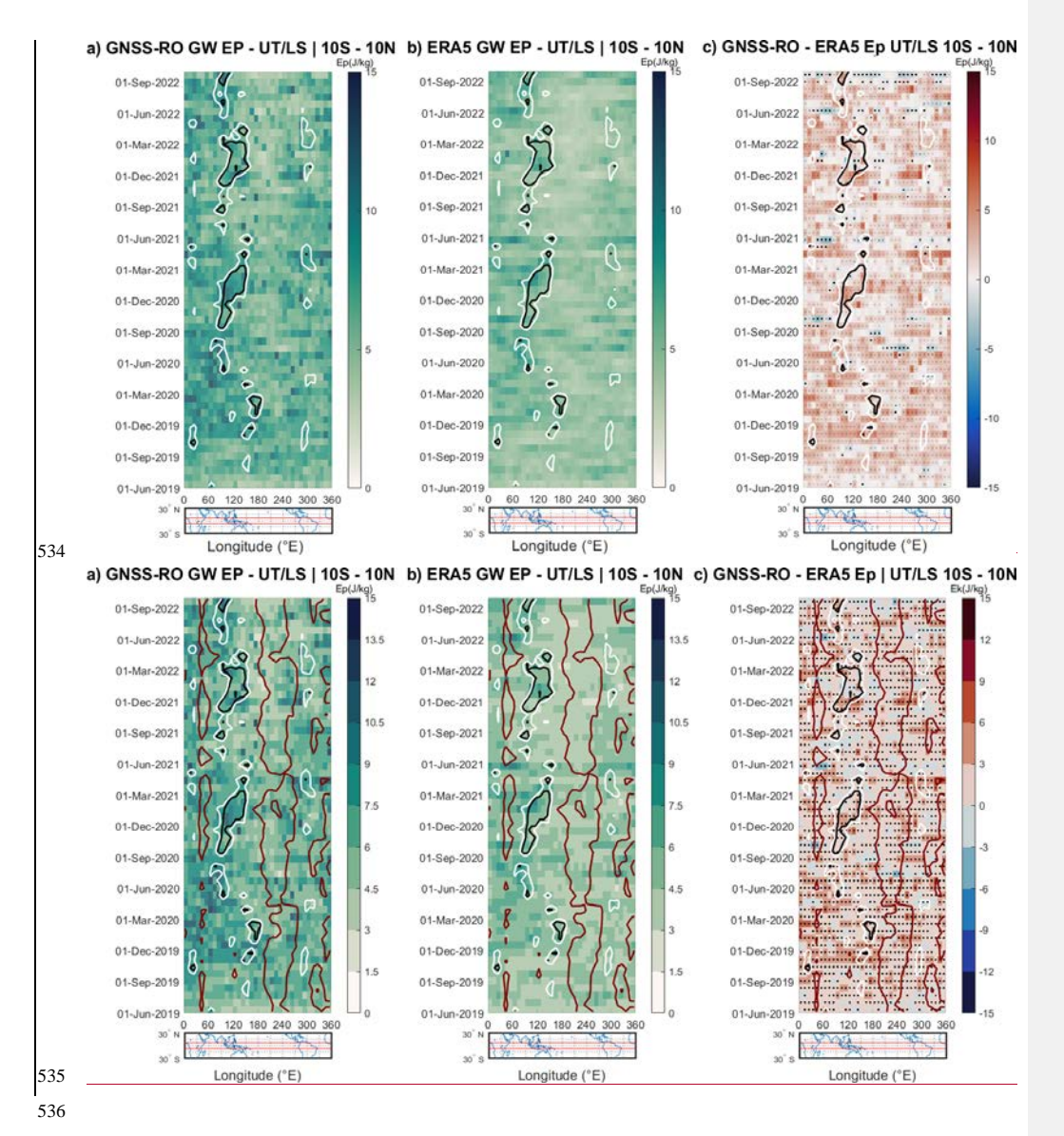


Figure 6. (a,b,c) Hovmoller diagram of Ep<sub>GNSS-RO</sub>, Ep<sub>ERAS</sub> and their difference White, black and red contour lines represent 210, 538 220 and 265 W/m2 OLR, respectively. The contour plot represents the Outgoing Longrange Radiation (OLR) for 210 and 220 W/m2 539 (black and white, respectively). Each bin corresponds to an average of over 3 weeks and 10 degrees. The OLR measurements were obtained from the Australian Bureau of Meteorology. The UTLS altitudes are defined between one kilometer below the tropopause 541 and 22 km. The tropopause is determined from the ERA5 reanalysis. Black stippling indicates regions where the difference between 542 quantities is statistically significant (two-sample t-test, p < 0.05).

543 The Ep<sub>GNSS-RO</sub> shown in Fig.6a does not closely follow the patterns of OLR activity. As the method employed removes most 544 traces of kelvin waves in the signal, the remaining activity is mostly comprised of GWs. This suggests that Ep does not 545 effectively capture GW activity in regions of deep convection, as indicated by the lowest OLR values. However, it is found 546 that the lesser\_non\_convective areas are seen both on instances of Ek and Ep, in Fig.3a and Fig.6a (with notable examples such as August 2020 around 100°E, as well as in May 2021 and 2022 near 50°E). This observation supports the notion that, in terms 547 548 of GW activity, deep convective phenomena primarily generate Ek, while less intense convective events (indicated in Fig.6a 549 as occurring in the neighbouring region outside the white contours) produce a more balanced distribution between both energy 550 components. It would be incorrect to assume that no wave activity occurs in low OLR regions; previous studies have shown that Ep values peak at 15 km altitude around the maritime continent, where the Walker circulation rises under non-El Niño 551 conditions (Ern et al., 2004; Yang et al., 2021). 552

555 Nonetheless, the Ep<sub>ERAS</sub> diagram shown in Fig.6b is generally consistent with the results shown in Fig.6a, if one admits that the instrumental signal is prone to more noise and higher average values. Particularly in regions outside the primary convection hotspots, in August 2020 around 100°E, we see coherent signals in both datasets. Similarly, in May 2021 near 50°E or in February 2022 near 120°E, distinct patterns emerge in both datasets. These alignments indicate that when gravity waves have 558 a stronger potential energy component, both datasets capture these features, even outside the primary zones of low OLR. It can also be noted that the patterns visible in Fig.6b strongly resemble the patterns presented by ERA5 in Fig.3b, a sign of ERA5's tendency to rely on the existence of Ep to determine the presence of Ek.

553 554

556

557

559

560 561

562 563

564

565

566

567

568

569

570

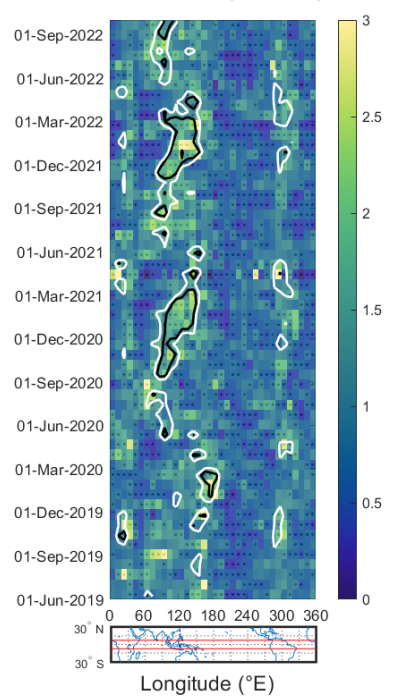
571

The differences between ERA5 and GNSS-RO data, depicted in Fig. 6c, show a mean absolute difference of 1.96 J/kg. This reflects a reasonable agreement, given that ERA5 assimilates GNSS-RO measurements. While there is a slight positive mean bias of 1.68 J/kg (GNSS-RO > ERA5), which accounts for the prevalence of light red colors in the plot, the differences are scattered and show no large-scale, systematic pattern correlated with convection. This stands in stark contrast to the systematic and large discrepancies observed in the kinetic energy fields.

The Ek differences are not only larger in magnitude, with a standard deviation nearly twice that of Ep (3.16 J/kg vs. 1.82 J/kg) and a maximum underestimation by ERA5 that is almost three times greater (>24 J/kg vs. ~9 J/kg for Ep), but they are also structurally different. The Ek difference plot is dominated by large, cohesive regions of statistically significant positive values (red), indicating a systematic underestimation by ERA5. While some areas do show a negative difference (blue color), these 572 are of small magnitude and, as confirmed by the lack of stippling, are not statistically significant. Most importantly, the peak 573 underestimation of Ek is systematically co-located with the deepest convective regions (inside the low OLR contours), whereas 574 the minor differences in Ep show no such alignment. Taken together, this evidence points to a specific limitation in the 575 reanalysis: the issue is not a general failure to represent wave energy, but a targeted inability of the model's physics and data 576 assimilation system to generate the intense, localized kinetic component of gravity waves originating from strong convection 577 in data-sparse regions. 578 The differences between ERA5 and GNSS RO data, depicted in Fig.6c, are minimal, with a mean absolute difference of 579 approximately 1.5 J/kg. This close agreement is expected, given that ERA5 assimilates GNSS RO temperature profiles. This 580 result demonstrates that the reanalysis system successfully reproduces the observed potential energy field. This finding stands 581 in sharp contrast to the significant underestimation of kinetic energy by ERA5 when compared to Aeolus observations (as 582 shown in Fig 4c). The combination of these results (good agreement in assimilated Ep and poor agreement in unassimilated 583 Ek) points to a specific limitation in the reanalysis's ability to model the kinetic component of convection induced gravity 584 waves, particularly in regions where direct wind observations are sparse.

 $586 \quad \text{An alternative display of Fig.6c as a ratio, along with an F-test, can be found in Appendix E.} \\$ 

# Aeolus Ek / GNSS-RO Ep | UT/LS | 10S - 10N



# Aeolus Ek / GNSS-RO Ep | UT/LS | 10S - 10N

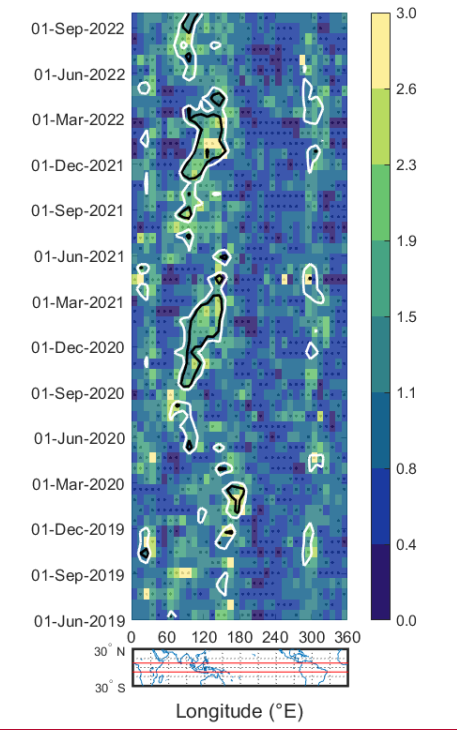


Figure 7. Relationship between  $Ek_{Aeolus\,HLOS}$ , and Ep from GNSSRO. The UTLS altitudes are defined between one kilometer below the tropopause and 22 km. The tropopause is determined from the ERA5 reanalysis. The tropopause is determined from the ERA5 reanalysis. Black stippling indicates regions where the difference between quantities is statistically significant (F-test, p < 0.05).

Fig. 7 presents the first observationally-derived long-term study of the Ek/Ep ratio, comparing Aeolus's HLOS Ek and GNSS-RO-derived Ep. It illustrates the longitudinal and temporal variations of the Ek/Ep ratio across the equatorial band ( $10^{\circ}$ S to  $10^{\circ}$ N) from June 2019 to October 2022.

The regions with the highest ratio values are systematically co-located with areas of deep convection, as indicated by the low OLR contours. This is particularly evident over the Indian Ocean (e.g., September-June 2019/20, 2020/21, and 2021/20) and

599 over the Western Pacific. This observation suggests that, in areas with similar seasonal characteristics, gravity waves tend to 600 transport more kinetic energy during convective events, which amplifies their influence on the overall energy dynamics. The 601 periodic patterns observed in the data also hint at a seasonal component previously observed by Zhang et al. (2010), potentially 602 tied to atmospheric phenomena such as the shifting ITCZ or changes in jet stream dynamics (Hei et al., 2008). These seasonal 603 fluctuations in the Ek/Ep ratio further reinforce the notion that gravity wave behavior is not static but is influenced by broader 604 atmospheric cycles (Ern et al., 2018; Zhang et al., 2010), contrary to the traditional linear theory paradigm in the literature. 605 Statistical significance testing (represented by the black stippling) confirms that these hotspots of high, convection-linked ratios are statistically significant features rather than artifacts. 606

- A significant division between the Indian Ocean and the eastern Pacific, marked by a contrast around 200° longitude, can be noted in both Fig.7 and Fig.4. This contrast reflects underlying geographic factors, including the distribution of large land masses orographic influences and convective activity. These two factors play a role in the generation and propagation of gravity waves, causing the distinct variations in the ratio between the two energies.
- This observational result stands in contrast to the picture presented by the ERA5 reanalysis in Fig.4. While ERA5 also shows variability in its Ek/Ep ratio, its regions of highest ratio are often located outside the main convective centers. This suggests
- that ERA5 misrepresents the physical link between deep convection and the partitioning of wave energy.

covariances fail to create the intense, localized kinetic energy associated with convective gravity waves.

- Given that ERA5 successfully assimilates GNSS-RO measurements, specifically bending angles which contain temperature information temperature data (and thus has a reasonable representation of Ep), this discrepancy points to a fundamental difficulty in the reanalysis's ability to generate the corresponding kinetic energy component in the right locations. Without direct wind profile assimilation in these data-sparse convective regions, the model's parameterizations and background error
- 629 However, it is noteworthy that in some specific regions and periods, such as over the Indian Ocean between June and 620 September of 2019, or in the longitude band around 300°E, a degree of correspondence between the model and observations 621 can be found. This suggests that for certain regimes, the reanalysis can approximate the energy partitioning, but it fails 622 systematically in the most intensely convective areas. These findings reinforce that direct kinetic energy measurements, as 623 provided by Aeolus, are essential for correcting model biases and improving our understanding of the gravity wave energy 624 budget.

625

#### 5. Discussion

626

- Overall, the results presented in this study allow us to discuss and address two main questions. The first consistent observation made, was that ERA5 underestimates Ek distribution in such regions compared to the Aeolus-derived energy, particularly over the Indian Ocean, where conventional radiosonde wind measurements are very sparse. That difference raised questions on the potential reason for such discrepancies: Is this result an overestimation of Aeolus, due to its known increased noise and inconsistent decaying performance during its life-cycle, or an underestimation for ERA5, due to the lack of direct wind
- 632 observations assimilated?
- 633 The analysis of ALADIN wind profiling and ECMWF ERA5 reanalysis data, provided in Fig.2 and Fig.3, revealed enhanced
- 634 GW activity over the Indian Ocean during Boreal Summer, as well as over the western Pacific and maritime continent in Boreal
  - Winter. The migration of this enhanced GW activity from eastern Africa to the Pacific maritime continent follows a
- clear seasonal cycle, strongly linked to deep convection as shown by the correlation with regional OLR minima. This robust
- 637 seasonal pattern indicates that the underlying wave sources are organized by planetary-scale phenomena, primarily the major
- 638 tropical monsoon systems (Wright and Gille, 2011). The structures observed by Aeolus are therefore highly consistent with
- the kinetic energy signature of gravity waves generated by the powerful thermal and mechanical forcing mechanisms (Beres
- 640 et al., 2005; Corcos et al., 2025) known to occur within the large, organized convective systems of the Asian, African, and
- 641 Maritime Continent monsoons (Kang et al., 2017; Liu et al., 2022). Previous satellite climatologies have firmly established
- 642 these monsoon regions as dominant global hotspots for stratospheric gravity wave activity (Hindley et al., 2020; Wright and
- 643 Gille, 2011). This suggests that Aeolus is effectively capturing these seasonally-driven, convection-induced GWs that are
- 4644 underrepresented in ERA5. One of the persistent features observed throughout the study was the high-energy gravity wave
- 645 hotspot over the African continent, which remained consistent across seasons and years. This suggests a continuous mechanism
- of continental convection driving gravity wave activity in this region.
- 647 The analysis of ALADIN wind profiling and ECMWF ERA5 reanalysis data, provided in Fig.2 and Fig.3, revealed enhanced
- 648 GW activity over the Indian Ocean during Boreal Summer, as well as over the western Pacific and maritime continent in Boreal
- 649 Winter. The enhanced GW activity migrating from eastern Africa to the Pacific maritime continent between June and
- 650 December is linked to convection, as suggested by the correlation between enhanced GW Ek and the regional minima in OLR.
- 651 The slow eastward propagation of these energy maxima suggests that the underlying wave sources are not random, but are
- 652 organized by planetary scale atmospheric patterns. Indeed, the relation between OLR and the Madden Julian Oscillation
- 653 (MJO) has been used before; It is a reliable index for analysis (Kiladis et al., 2014), and recent work has provided direct
- 654 observational evidence that the MJO modulates GW activity and momentum transport from the tropics to higher
- 655 latitudes (Zhou et al., 2024). The structures observed by Aeolus are therefore highly consistent with the kinetic energy signature
- 656 of gravity waves generated by the powerful thermal and mechanical forcing mechanisms (Beres et al., 2005; Corcos et al.,
- 657 2025) occurring within the large, organized convective superclusters of the MJO. This suggests that Aeolus is effectively

658 capturing convection induced GWs that may be underrepresented in ERA5. One of the persistent features observed throughout
659 the study was the high energy gravity wave hotspot over the African continent, which remained consistent across seasons and
660 years. This suggests a continuous mechanism of continental convection driving gravity wave activity in this region.

661 Another consideration in this study is whether the large Ek values observed by Aeolus, particularly over convective hotspots, 662 could be an artifact of misinterpreting non-wave tropospheric outflow rather than stratospheric gravity waves. Our sensitivity 663 analysis (see Fig. B1 and B2 in Appendix B) directly refutes this concern. By shifting the analysis layer upward to begin 1 km 664 and 2 km above the tropopause, we confirm that the geographical patterns of the energy hotspots are remarkably stable (spatial correlation r > 0.83), and that the vast majority of the peak energy (~88-91%) persists well into the stratosphere. If the signal 665 666 were dominated by shallow tropospheric outflow, the energy peaks would have collapsed when the analysis layer was moved 667 above the tropopause. The fact that a strong, structured signal remains provides compelling evidence that we are observing 668 vertically propagating gravity waves that have penetrated the lower stratosphere. This validates our central conclusion: Aeolus is capturing a significant field of convectively generated stratospheric gravity wave kinetic energy that is largely absent in the 669 670 ERA5 reanalysis.

Having established that the Aeolus kinetic energy signal is robust and represents vertically propagating stratospheric gravity
waves rather than tropospheric artifacts (as confirmed by our sensitivity analysis in Sect. 2.2), we can use external information
to arbitrate the cause of the discrepancy with ERA5. An additional tool at our disposal to solve the case is the global distribution
of Ep, through the use of independent GNSS-RO instruments. Our analysis confirms that the assimilation of GNSS-RO data
in ERA5 is highly effective, with minimal discrepancies observed between the reanalysis Ep and direct GNSS-RO observations
(Fig.6c). This key finding allows us to arbitrate between two potential causes for the Ek discrepancy: a lack of direct wind data
assimilation versus inherent biases in the model's physics (e.g., its GWD parameterization).

Several lines of evidence from our study point towards the lack of wind assimilation as the dominant cause. Firstly, the fact that ERA5 accurately reproduces Ep fields demonstrates that the underlying model can represent the thermodynamic signatures of wave activity when properly constrained. Conversely, the largest discrepancies are found in kinetic energy, a purely wind-based quantity, and are concentrated over data-sparse regions like the Indian Ocean, precisely where Aeolus provides direct wind profile measurements not available from other observing systems (Banyard et al., 2021).

Secondly, while ERA5's non-orographic GWD scheme has known limitations and is not directly forced by diagnosed convection (Orr et al., 2010), it is unlikely to be the sole reason for the missing Ek. Such a parameterization bias would be expected to manifest as a systematic error across different variables or regions, or as a persistent model drift requiring large, ongoing corrections by the assimilation system (Dee, 2005). However, our findings show a targeted deficiency: the model performs well on assimilated temperature (Ep) but poorly on unassimilated wind (Ek) in the very same locations. This sharp contrast strongly suggests the problem is not a wholesale failure of the model's physics to generate wave energy, but rather its inability to correctly partition that energy into kinetic and potential components without direct wind constraints.

690 In data-sparse areas, ERA5 must rely on its internal background error covariances to infer wind adjustments from the 691 assimilated mass field (Hersbach et al., 2020). These statistical relationships are primarily designed to represent large-scale, 692 quasi-balanced (rotational) flow and have long been known to be less effective at specifying the smaller-scale, divergent 693 component of the wind field to which convectively generated gravity waves belong, especially in the tropics (Žagar et al., 694 2004). While the Integrated Forecasting System (IFS) has evolved considerably, recent Observing System Experiments (OSEs) 695 using Aeolus data confirm that this challenge persists. These studies provide direct evidence that the assimilation of Aeolus 696 wind profiles systematically enhances the analyzed amplitudes of equatorial waves, particularly in regions of strong vertical wind shear where the model's background state is most uncertain (Žagar et al., 2021, 2025). Consequently, while the 697 698 assimilation of GNSS-RO constrains the thermodynamic (Ep) aspect of the wave, the system lacks the necessary information 699 and dynamic constraints to generate the corresponding divergent wind perturbations, leading to the observed Ek deficit. This 700 process evidently fails to capture the full spectrum of high-Ek wave modes generated by convection. These statistical 701 relationships are primarily designed to represent large-scale, quasi-balanced (rotational) flow and are known to be less effective 702 at specifying the smaller scale, divergent component of the wind field to which convectively generated gravity waves belong, 703 especially in the tropics (Žagar et al., 2004). Consequently, while the assimilation of GNSS-RO constrains the thermodynamic 704 (Ep) aspect of the wave, the system lacks the necessary information and dynamic constraints to generate the corresponding 705 divergent wind perturbations, leading to the observed Ek deficit. This process evidently fails to capture the full spectrum of 706 high-Ek wave modes generated by convection.

Overall, the findings presented here are in full agreement with the elements outlined in the introduction, suggesting that ERA5

707

721

722

723

708 is underestimating the Ek component. Indeed, ERA5 has several known shortcomings, such as its underrepresentation of 709 eastward-propagating inertio-gravity waves (Bramberger et al., 2022), its site-dependent errors in tropical regions (Campos et 710 al., 2022), and the broader limitations of data assimilation systems in capturing circulation dynamics, particularly in areas with 711 sparse wind observations (Podglajen et al., 2014; Žagar et al., 2004). These challenges are particularly evident in the 712 representation of key tropical phenomena like the Quasi-Biennial Oscillation (QBO), which is driven by the upward 713 propagation and dissipation of a spectrum of atmospheric waves. Recent studies using direct Aeolus wind observations have 714 provided new insights into how reanalyses represent these processes. For instance, Banyard et al. (2023) found that during the 715 2019/2020 QBO disruption, a period covered by our study, the onset of the disruptive easterly jet was observed by Aeolus five 716 days earlier than in ERA5. This discrepancy was linked to higher Kelvin wave variances and sharper vertical wind shear in the 717 Aeolus data, suggesting that ERA5 may misrepresent the breaking of smaller-scale waves that are crucial for forcing the QBO. 718 Similarly, Ern et al. (2023) confirmed that while the zonal-mean QBO is well-represented in ERA5, local biases exist, 719 particularly in shear zones. From a data assimilation perspective, Zagar et al. (2025) showed that assimilating Aeolus winds 720 produced the largest changes to the analyzed state in the UTLS precisely during the 2019/2020 QBO disruption, highlighting

Mis en forme : Anglais (Royaume-Uni)

Mis en forme: Anglais (Royaume-Uni)

the importance of direct wind observations for reducing uncertainties in these critical shear zones. Together, these findings,

derived from the same novel wind dataset used here, support our conclusion that reanalyses can have significant deficiencies

in representing the full spectrum of wave activity and its associated kinetic energy in the absence of direct wind assimilation. These challenges are further emphasized by the OBO MJO modulation of the wave activity in the UTLS, possibly

726 compared to others. An observational study revealed how gravity waves generated during MJO phases interact with QBO-727 modulated wind patterns, influencing their dissipation and energy dispersion (Kalisch et al., 2018). The QBO easterly phase 728 (EQBO) has been shown to enhance MJO activity by strengthening convective signals and reinforcing the propagation of 729 Rossby and Kelvin waves in the UTLS, while the westerly phase (WOBO) suppresses these dynamics (Song and Wu, 2020; 730 Martin et al., 2021). However, the limitations of ERA5 in capturing OBO-MJO interactions are evident, as reanalysis datasets 731 often fail to fully reproduce the observed temperature and wind anomalies associated with these processes, particularly in 732 tropical regions (Lim and Son. 2022). 733 Another discussion enabled by Aeolus observations concerns the longstanding assumption of a constant Ek/Ep ratio in GW 734 studies. Specifically, the question arises: Is the conventional view of a constant ratio for inferring Ep from Ek (and vice versa) 735 still tenable? Or do the new data suggest that this ratio is no longer universally valid in real-world, often non-linear, atmospheric 736 conditions? 737 At first glance, using a fixed ratio appears straightforward for converting well-documented Ep (from temperature-based 738 instruments such as GNSS-RO) to Ek. Traditionally, linear GW theory proposes a near-constant ratio of Ek to Ep, often quoted 739 between 5/3 and 2.0 (VanZandt, 1985; Hei et al., 2008). In idealized models of linear wave behavior, the kinetic and potential 740 energies are expected to be comparable, leading to a ratio close to unity. This theoretical relationship has been confirmed 741 observationally. In stable, linear wave conditions, the energy ratios adhere closely to predictions (Nastrom et al., 2000), a 742 finding supported by a modern case study of individual, freely-propagating waves (Huang et al., 2021). 743 However, a growing body of evidence challenges this simplification: Empirical work increasingly reveals significant 744 variability in this ratio, indicating non-linear effects in real-world atmospheric conditions (Wing et al., 2025; Baumgarten et al., 2015; Guharay et al., 2010; Tsuda et al., 2004). When the observed energy ratios deviate significantly from this expected 745 746 range, non-linear processes may be at play. While a large climatological study may find a mean Ek/Ep ratio close to theoretical 747 values (e.g., 1.5 in Zhang et al., 2022), this average can mask significant event-to-event variability. For instance, in situations 748 where wave amplitudes are particularly large, wave-wave interactions, such as those resulting from wave breaking or 749 saturation, could lead to the observed discrepancies. This has been demonstrated in earlier work by Mack and Jay. (1967), who 750 found that under certain conditions, potential energy deviated markedly from kinetic energy, suggesting non-linear effects. 751 Similar findings have been reported by Fritts et al. (2009), who showed that interactions between gravity waves and fine 752 atmospheric structures can result in turbulence, thereby affecting the balance between kinetic and potential energy. A recent 753 study also confirmed that the ratio is not static and can be actively modulated by the background atmospheric state, such as

at play in the amplitude variability of the seasonal signals seen in Fig.3a, where some years show an increased activity

725

754

strong wind shear (Wing et al., 2025).

At first glance, using a fixed ratio appears straightforward for converting well-documented Ep (from temperature based instruments such as GNSS-RO) to Ek. Traditionally, linear GW theory proposes a near-constant ratio of Ek to Ep, often quoted between 5/3 and 2.0 (VanZandt, 1985; Hei et al., 2008). In idealized models of linear wave behavior, the kinetic and potential energies are expected to be comparable, leading to a ratio close to unity. This has been confirmed previously, in a study such as Nastrom et al. (2000), which found that in stable, linear wave conditions, the energy ratios adhered closely to these theoretical predictions.

761 However, a growing body of evidence challenges this simplification: Empirical work increasingly reveals significant variability in this ratio, indicating non-linear effects in real-world atmospheric conditions (Baumgarten et al., 2015; Guharay 762 763 et al., 2010; Tsuda et al., 2004). When the observed energy ratios deviate significantly from this expected range, non-linear 764 processes may be at play. For instance, in situations where wave amplitudes are particularly large, wave wave interactions, 765 such as those resulting from wave breaking or saturation, could lead to the observed discrepancies. This has been demonstrated in earlier work by Mack and Jay, (1967), who found that under certain conditions, potential energy deviated markedly from 766 767 kinetic energy, suggesting non linear effects. Similar findings have been reported by Fritts et al. (2009), who showed that 768 interactions between gravity waves and fine atmospheric structures can result in turbulence, thereby affecting the balance 769 between kinetic and potential energy.

GNSS-RO confirms that the characteristics of gravity waves vary significantly across time and space. The observed ratios, 1.7 (+/- 0.38) for ERA5, 1.4 (+/- 0.54) for Aeolus/GNSS-RO, indicate that the waves encompass both linear and non-linear processes. The frequent observation of ratios exceeding unity, aligning with trends identified in previous studies, suggests that a substantial portion of the waves' energy is contained in kinetic form, often indicative of non-linear behavior. Because the assumption of a constant ratio is increasingly challenged by empirical observations (see references in the previous paragraph), it accentuates the need to shift the paradigm from relying solely on temperature perturbations to directly deriving Ek. As such, directly measuring kinetic energy is a major missing link for a comprehensive understanding of GW dynamics.

With everything in place to link these elements, the observed comparison in Fig.4 of the Ek/Ep ratios from ERA5, Aeolus, and

770

771

772

773

774

775

776

777

Beyond these considerations of gravity wave dynamics and energy ratios, we should also acknowledge the limitations of the
Aeolus satellite. These include both its technical shortcomings and the constraints imposed by its HLOS projection, which
directly impact the representativeness of its measurements. A 1.6 ratio was determined for Ek/Ek<sub>HLOS</sub> using ERA5, as seen in
Fig.2 (as detailed in Sect. 2.2 and shown in Appendix C). It reflects the efficiency with which HLOS winds from Aeolus can
approximate the full kinetic energy field. The ratio indicates that HLOS winds account for approximately 62.5% of the total
Ek, while the remaining 37.5% is undetectable due to the projection limitations of HLOS measurements. The discrepancy
suggests that the HLOS winds alone cannot fully capture the energy contributions from multi-dimensional wave dynamics.

785 However, this ratio can help estimate the full Ek indirectly with reasonable accuracy. While this approach introduces some 786 assumptions, it can be further refined by cross-validating against comprehensive datasets from reanalyses like ERA5.

787

788

789

790

791

792

793

794

795

796 797

798

799

800

801

802

803

804

805

806

807

808 809

810

811

813

815

The spatial and temporal consistency observed between Aeolus and ERA5 datasets highlight the potential of Aeolus wind profiling for assimilation to improve our understanding of atmospheric dynamics in the tropical UTLS. However, there are limitations and uncertainties to consider; these include dark currents in its charge coupled devices, known as "hot pixels". which can induce speed measurement errors of several meters per second (Weiler et al., 2021). Additionally, oscillating perturbations within the instrument can cause signal deformations, potentially misinterpreted as GW induced signals (Ratynski et al., 2023). Even though corrections have been implemented, Fig.3 showed that the instrument's overall signal random error still fluctuates due to its degradation. While newer baselines such as the latest 2B16 used in this study, improve on the appearance rate of hot pixels, challenges remain in consistently identifying and correcting other issues such as oscillating perturbations, increased solar activity, or cloud contamination that can sporadically deform signals.

Aeolus is inherently limited in retrieving accurate vertical wavelengths due to its design. The placement of range bins was fixed at the time of observation, introducing inconsistencies in vertical resolution that affect the precise identification of wave peaks and troughs. Additionally, the N/P parameter, which controls the number of accumulated measurements (N) and pulses (P) per cycle, introduces variability in the horizontal resolution of Aeolus data. Changes to this setting, such as the transition from N=30 to N=5, improve horizontal resolution but exacerbate the misrepresentation of vertical wave structures. Furthermore, any spectral analysis of a finite vertical profile is inherently constrained. For geophysical spectra that are typically having more variance at longer wavelengths, a simple peak-finding method would likely identify a dominant wavelength that is an artifact of the analysis window or filtering choices. Given these limitations, we limit our analysis to the verticallyintegrated energy within a defined-band-pass filter (vertical wavelengths between 1.5 and 9 km) passband (vertical wavelengths < 9 km), which is a more robust quantity.

Understanding the vertical wavelength of convective GWs is an essential element for characterizing their dynamics. However,

Nevertheless, we can speculate that the high Ek values observed by Aeolus in convective regions are associated with shorterwavelength waves. This interpretation is consistent with established physical mechanisms which state that waves with high EK are typically generated in regions with strong convective updrafts and downdrafts, where the rapid vertical movement of 812 air masses creates intense small-scale disturbances. These localized and transient disturbances, arising from geostrophic imbalance, generate GWs that carry energy away from the convective region, where strong forcing efficiently transfers energy 814 into the EK spectrum at shorter wavelengths (Waite and Snyder, 2009). The correlation between high EK and shorter wavelengths is particularly pronounced in convective systems, as confirmed in both observational and numerical estimations 816 (Kalisch et al., 2016), especially in tropical regions and cyclones (Chane Ming et al., 2014). A definitive observational

817 confirmation of this from the satellite itself, however, remains a challenge due to the aforementioned limitations. Mis en forme: Police: (Par défaut) Times New Roman, 10 pt, Couleur de police : Automatique, Motif : Transparente

819 essential for global circulation models. However, deriving momentum flux estimates directly from single-820 component wind measurements like those from Aeolus presents two co-dependent problems. First, the vertical flux of 821 horizontal momentum (e.g., (u'w')) requires simultaneous knowledge of horizontal (u') and vertical (w') wind perturbations. 822 Aeolus supplies only the line-of-sight projection of the horizontal wind and, crucially, no direct information on the vertical 823 wind. In the standard processing w' is simply assumed negligible (Krisch et al., 2022), leaving the key term in the flux equation 824 unconstrained. Second, the satellite's sampling geometry further limits what can be inferred. Aeolus observes with a ~3 km-825 wide "pencil beam" that is horizontally averaged to about 86 km along track, and its sun-synchronous orbit completes ~16 826 revolutions per day (roughly 32 equator crossings, or 15-16 every 12 h). Small-scale gravity waves are therefore captured only 827 where the narrow ground tracks happen to intersect them, leaving large spatial and temporal gaps. Together, the absence of 828 direct w' measurements and this sparse, one-dimensional sampling mean that Aeolus winds alone cannot yield global 829 momentum-flux maps without substantial modelling support or complementary observations. 830 Looking forward, a critical application for such observations is the constraint of gravity wave momentum fluxes, which are 831 essential for global circulation models. However, deriving momentum flux estimates directly from single-832 component wind measurements like those from Aeolus presents significant theoretical and observational challenges. The 833 vertical flux of horizontal momentum (e.g., \(\sqrt{u}\)') fundamentally requires simultaneous knowledge of both horizontal \((u\)') and 834 vertical (w') wind perturbations. Aeolus provides only a projection of the horizontal wind and, crucially, contains no direct 835 information on the vertical wind; in fact, w' is assumed to be negligible in the standard data processing (Krisch et al., 2022). 836 This represents the primary missing piece of information for a direct flux calculation. 837 A potential pathway to overcome this limitation involves creating synergistic datasets, for instance by combining Aeolus wind 838 data with simultaneous, collocated temperature measurements from instruments like GNSS-RO. In principle, gravity wave 839 polarization relations could then be used to infer the missing wind components. However, this approach is not a simple remedy 840 and relies on strong, often unverifiable, assumptions about unmeasured wave parameters, including the horizontal wavelength, 841 intrinsic frequency, and the stationarity of the wave field between measurements (Alexander et al., 2008a; Chen et al., 2022). 842 Therefore, while Aeolus does not directly measure momentum flux, its unprecedented global measurements of kinetic energy 843 provide an additional observational constraint. Such observations are a critical prerequisite for developing and testing the more 844 complex, multi-instrument techniques that will be required to eventually constrain the global gravity wave momentum budget.

Looking forward, a critical application for such observations is the constraint of gravity wave momentum fluxes, which are

818

#### 6. Conclusion

845

853

854

855

858 859

860

861

862 863

864

865

866

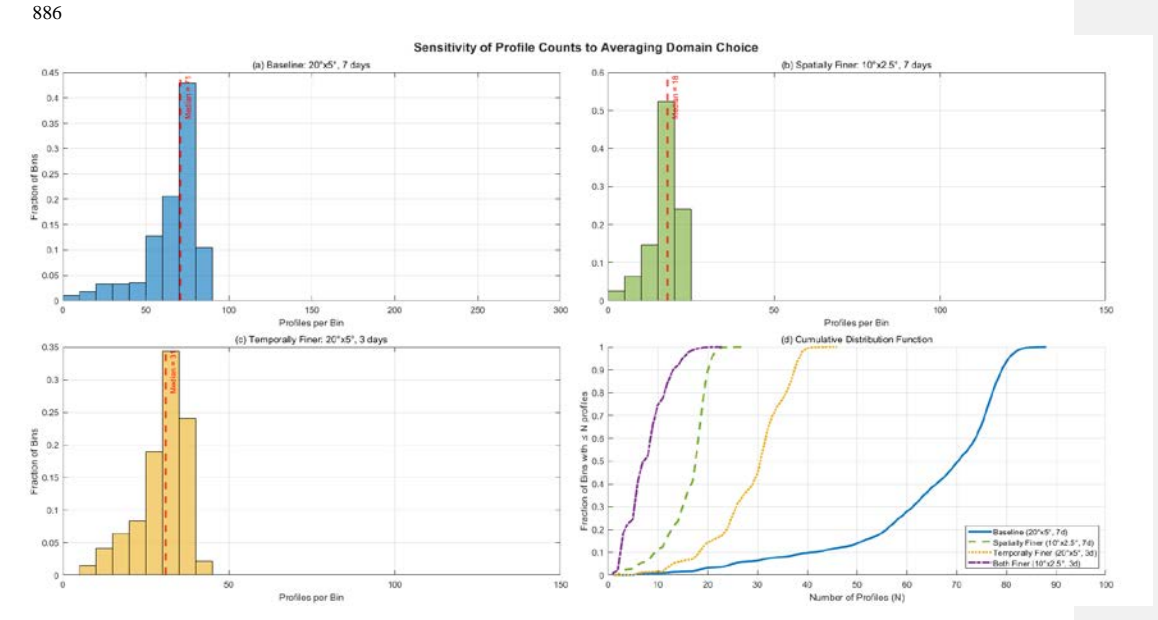
867

868

- 846 In this study, we examined the capacity of the Aeolus ALADIN instrument to capture and resolve GWs in tropical UTLS.
- 847 While this task might appear challenging at first, because of the data alteration issues Aeolus faced during its lifecycle, the
- 848 study proposed a noise correction process, which used ERA5 reanalysis as a reference to estimate and correct for Aeolus's
- 849 instrument-induced variance. This correction improved the retrieving of kinetic energy, and our comparison with collocated
- 850 radiosonde data further validated that approach. A key focus of our analysis was the ratio between kinetic and potential energies
- 851 (Ek/Ep), providing insights into the linear or non-linear nature of these waves.
- 852 The principal findings can be summarized as follows:
  - Aeolus observations capture significant kinetic energy enhancements over tropical convection hotspots, particularly
    over the Indian Ocean, where ERA5 shows substantial underrepresentation due to sparse wind observations.
- Direct wind data from Aeolus could significantly enhance tropical UTLS reanalysis products, particularly in
   convection-driven GW regimes, reducing biases in Ek representation.
  - In many regions with strong convective forcing, Aeolus data suggest a larger kinetic energy component, pointing to
    wave breaking, saturation, and other non-linear processes that depart from purely linear wave dynamics.
  - While linear GW theory often prescribes an Ek/Ep ratio between ~1.6 and ~2.0, our results show that this ratio can
    vary significantly, depending on location and season. This highlights the need for direct kinetic-energy measurements
    rather than relying solely on temperature-derived potential energy as a proxy.
  - Aeolus also helps fill this gap. However, given its HLOS projection, Aeolus underestimates the total Ek if meridional
    components are significant, reinforcing that multi-instrument approaches are mandatory for accurately characterizing
    GW fields.
- Thus, this study has demonstrated the value of Aeolus Rayleigh wind profiling for observing GWs in the tropical UTLS, despite the high and time-variable random error associated with its measurements. Our findings confirm that the annual and zonal variation of GW activity in the tropical tropopause layer and lower stratosphere is modulated by deep convection, as demonstrated by Dzambo et al. (2019) and Evan et al. (2020). Furthermore, Aeolus data expose a significant need for improving the reanalysis regarding the convective GW Ek. The lack of GW-derived Ek in ERA5 is most pronounced in the Indian Ocean region, where conventional radiosonde wind measurements are relatively sparse. It is highly likely that the missing Ek in ERA5 is due to the misrepresentation of convective processes. The results also indicate that standard assumptions

about the Ek/Ep ratio do not always hold, particularly under convective or otherwise non-linear conditions. Aeolus' range-bin design and horizontal integration restrict its ability to determine wavelengths with accuracy, which poses a significant challenge for fully capturing the characteristics of GW. This limitation highlights the need for complementary datasets, which could be addressed in newer iterations of the instrument. While this study delivers some insights into UTLS GW activity and the benefits of global wind observation, future research should continue investigating the factors contributing to the discrepancies observed between Aeolus and ERA5 data. The kinetic energy constraints provided here represent a novel step, and future missions like Aeolus-2 will be essential for developing the synergistic techniques required to ultimately quantify the global momentum transport by these waves.

### 885 Appendix A : Sensitivity Analysis



887 Figure A1. Sensitivity of Aeolus profile counts per analysis bin to the choice of spatio-temporal averaging domain.

Figure A1 presents the histograms of the number of Aeolus profiles available per spatio-temporal bin for four different averaging domain configurations: (a) the baseline 20°x5°, 7-day domain used in this study, (b) a spatially finer 10°x2.5°, 7-

day domain, and (c) a temporally finer 20°x5°, 3-day domain. Red dashed lines indicate the median profile count for each configuration. Panel (d) shows the cumulative distribution function for all four configurations, including a domain that is finer in both space and time. The results demonstrate the trade-off between domain size and sampling density. While finer domains offer higher resolution, they significantly reduce the number of profiles available for robustly calculating the background state, with a majority of bins containing fewer than 20 profiles. The baseline configuration (blue line) was chosen as it ensures a sufficient number of profiles per bin (median of 71) to minimize noise and provide a stable background estimate, as discussed in the main text.

### 897 Appendix B: Aeolus sensitivity to the tropopause selection

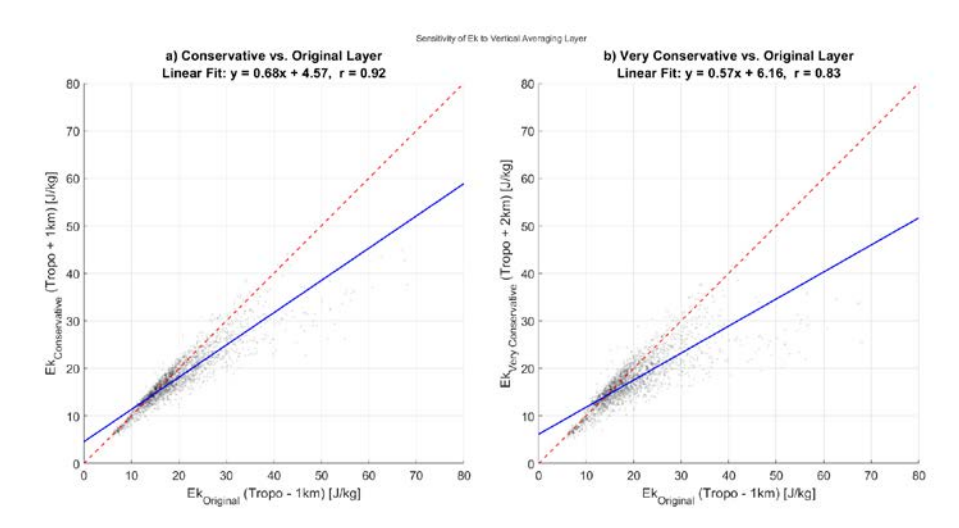


Figure B1. Scatter plot comparison of Aeolus-derived kinetic energy (Ek) calculated using different vertical averaging layers.

Figure B1 tests the sensitivity of the derived kinetic energy to the vertical averaging layer, addressing the potential contamination from upper-tropospheric non-wave outflow. The x-axis on both panels represents the Ek calculated using our original layer (starting 1 km below the tropopause). (a) The y-axis shows Ek calculated using a "Conservative" layer starting 1 km above the tropopause. (b) The y-axis shows Ek from a "Very Conservative" layer starting 2 km above the tropopause. The strong linear correlation (r = 0.92 and r = 0.83, respectively) and the fact that the data points cluster near the 1:1 line (red dashed line) demonstrate that the majority of the energy signal is retained when the upper troposphere is excluded. The linear

fit (blue solid line) shows a predictable reduction in magnitude but confirms that the underlying spatial patterns of high and low energy are highly consistent across all layers.

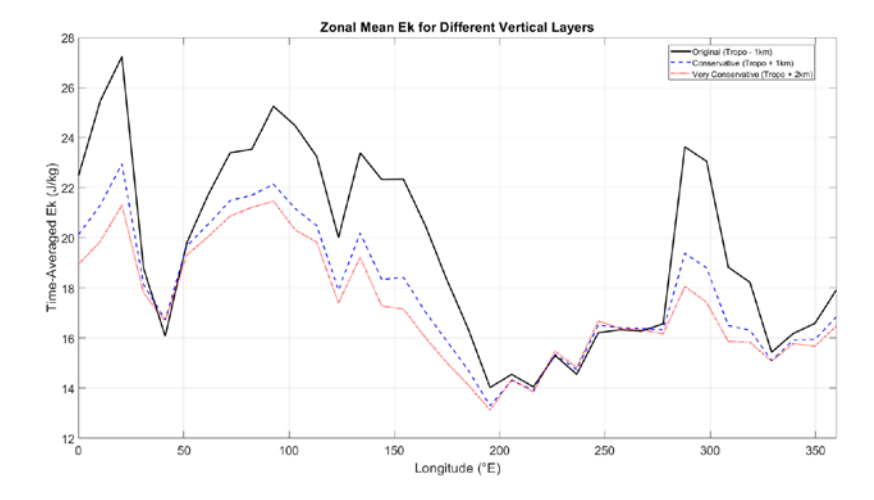


Figure B2. Zonal mean structure of time-averaged Aeolus kinetic energy (Ek) for different vertical averaging layers.

Figure B2 shows the time-averaged, zonal mean Ek as a function of longitude for the three different vertical averaging layers defined in Figure B1. The black line represents our original layer, the blue dashed line is the "Conservative" layer (+1 km), and the red dotted line is the "Very Conservative" layer (+2 km). The plot confirms that while the absolute magnitude of Ek decreases as the layer is moved higher into the stratosphere (as expected due to wave dissipation), the geographical structure of the energy hotspots is remarkably stable. The primary peaks of high energy (e.g., over the African/Indian Ocean sector from ~60-120°E and the Americas/Atlantic sector from ~280-320°E) persist across all three calculations. This provides strong evidence that the observed energy hotspots are robust features originating from vertically propagating gravity waves that have reached the lower stratosphere, and not artifacts of shallow upper-tropospheric outflow.

# Appendix C : EK / EK\_HLOS Ratio

918

922

923

924

925

926

927

928

929

930

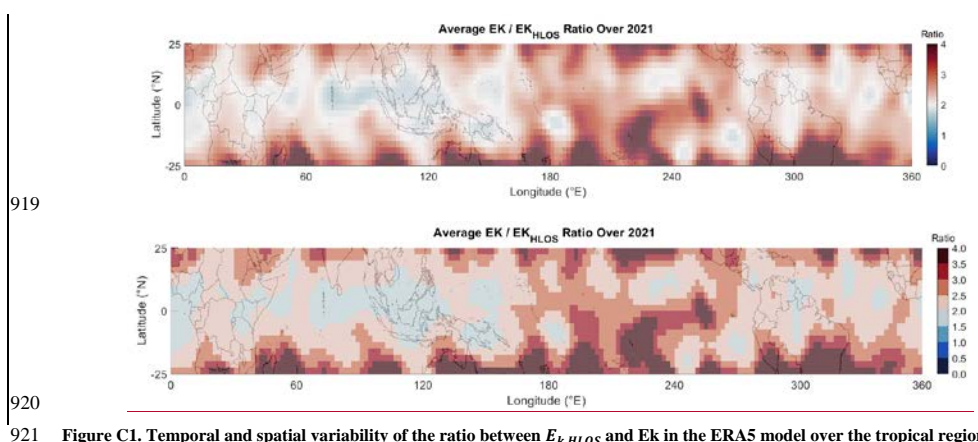


Figure C1. Temporal and spatial variability of the ratio between  $E_{k\,HLOS}$  and Ek in the ERA5 model over the tropical region (30°S–30°N) for the year 2021

Figure C1 displays the ratio between  $E_{k\,HLOS}$  and Ek in the ERA5 model, over the tropical region for the UTLS. The ratio values range from 1.5 to 3, between January 2021 and December 2021 included, depicting variations in how well the HLOS measurements capture the total kinetic energy in this region.

This map illustrates the anisotropy of the gravity wave field as represented in the ERA5 model for the year 2021, chosen for its significant wave activity which highlights the regional patterns of energy partitioning. The ratio quantifies the contribution of the unobserved meridional wind component to the total kinetic energy. A ratio of 1 (blue colors) indicates purely zonal wave energy, while higher values (red colors) signify an increasing contribution from meridional motions.

A distinct pattern emerges along the equatorial belt (10°S - 10°N). Over a vast longitudinal sector stretching from Africa, across the Indian Ocean, and over the Maritime Continent (approximately 0°E to 160°E), the ratio remains low, generally below 2.0. This indicates that wave energy is predominantly zonal in these regions, meaning a quasi-zonal HLOS measurement like that from Aeolus is expected to capture a large fraction of the total kinetic energy. This aligns with the influence of persistent large-scale zonal flows in this sector, such as easterly trade winds.

936 In contrast, the sector from approximately 160°E to 280°E, encompassing the central and eastern Pacific, shows significantly 937 higher ratios, often exceeding 2.5. This points to a wave field with a much stronger meridional component, where an HLOS 938 measurement would systematically underestimate the total kinetic energy. A third regime is observed over the Atlantic and Mis en forme : Centré

939 South America (from 280°E to 360°E), where the ratio is more variable but consistently elevated, indicating a mixed wave 940 field with a significant, though not always dominant, meridional energy component.

#### 942 Appendix D: Aeolus Instrumental Noise Correction Methodology

- This appendix provides a detailed, step-by-step description of the spatio-temporally adaptive algorithm used to correct for 944 time-varying instrumental noise in the Aeolus-derived gravity wave (GW) kinetic energy (Ek) data. The objective is to produce a corrected dataset,  $\overline{Ek_{Aeolus\,HLOS*}}$ , that removes instrumental bias while preserving the unique, high-fidelity geophysical 945 946 signals of GWs that Aeolus observes. The correction methodology involves two primary stages: first, a detailed correction 947 applied to time-longitude Hovmöller diagrams, and second, a refinement of this correction for application to broader
- 948 geographical maps.

941

943

950

#### 949 Part 1: Correction of Time-Longitude Hovmöller Diagrams

951 spatio-temporal and component estimates of this noise are derived, we will use the "hat" notation to explicitly denote these estimated noise values, such as  $\overline{Ek_{LN}}$  for the time-longitude noise estimate. The initial estimation of the noise term is 952 953 performed on the 2D Hovmöller data matrices of Aeolus  $E_{k,AeolusHLOS}(t,\phi)$  and ERA5  $E_{k,ERA5\;HLOS}(t,\phi)$  where t represents 954 time steps (3-week averages) and φ represents longitude bins. This correction is conducted within the 10°S-10°N latitude band 955 where deep tropical convection is most prominent. The algorithm adaptively estimates the instrumental noise component 956  $\overline{\mathrm{Ek}_{\mathrm{LN}}}$   $(t, \phi)$  which is then subtracted from the observed Aeolus energy as shown conceptually in Eq. (6) of the main text.

As introduced in the main text, our best estimate of the noise energy is denoted as  $\overline{Ek_{LN}}$ . Within this appendix, where specific

- Step 1: Defining an Activity-Based Blending Weight 957
- 958 The core of the adaptive algorithm is a blending weight,  $W(t, \phi)$ , that determines the balance between an additive and a 959 multiplicative correction approach. This weight is derived from the ERA5 Ek, which serves as a proxy for the true level of atmospheric GW activity. First, a background reference energy  $E_{R,bg}$  (bg standing for background) defined as the median 960 ERA5 Ek within a pre-defined quiescent reference sector (200°E-250°E over the Pacific Ocean), chosen for its typically low 961 962 convective activity. An activity index, x(t,L), is then computed for each point in the Hovmöller diagram:

963 
$$x(t, \phi) = \frac{E_{k,ERA5HLOS}(t, \phi) - E_{k,bg}}{E_{k,bg}}$$
(7)

From this index, a logistic function is used to create a preliminary activity map, A(t,L), ranging from 0 (quiescent) to 1 (active):

965 
$$A(t,\phi) = \frac{1}{1+e^{-x(t,\phi)}}$$
 (8)

967 To ensure spatial coherence and prevent abrupt transitions, this activity map is smoothed using a 2D Gaussian filter with a

968 standard deviation of 2 pixels in the time dimension and 10 pixels in the longitude dimension. The final background-confidence

969 weight, W(t,L), is then defined as:

966

971

981

986

988

990

970 
$$W(t,\phi) = 1 - A_{smoothed}(t,\phi)$$
 (9)

972 Thus, W is close to 1 in quiescent regions and approaches 0 in highly active regions.

#### 973 Step 2: Deriving the Additive and Multiplicative Correction Components

- 974 Two candidate correction components are calculated. The additive component is designed to correct for the baseline
- 975 instrumental noise offset. A time-dependent offset vector,  $\delta_{noise}(t)$ , is computed by taking the median difference between
- 976 Aeolus and ERA5 Ek within the same quiet reference sector used in Step 1:

977 
$$\delta_{noise}(t) = \text{median}_{\phi \in \text{ref. sector}} \left( E_{k,AeolusHLOS}(t, \phi) - E_{k,ERA5HLOS}(t, \phi) \right)$$
 (10)

- 978 This offset vector, which captures the time-varying instrumental bias trend, is then smoothed temporally with a 7-point (21-
- 979 week) moving median to reduce noise. The additively corrected energy field,  $E_{k,bias-adj}$  is then defined as:

980 
$$E_{k,bias-adj}(t,\phi) = E_{k,AeolusHLOS}(t,\phi) - \beta \cdot \delta_{noise}(t)$$
 (11)

- where  $\beta$  is an offset relaxation factor (set to 1.15) to empirically fine-tune the subtraction.
- 983 The multiplicative component is designed for active regions where noise effects might scale with the signal. A single, mission-
- 984 period Activity Ratio Scalar,  $\mathcal{R}_{\mathcal{A}/\mathcal{E}}$ , is computed as the median ratio of Aeolus to ERA5 Ek over all grid points where the
- 985 activity weight  $A(t,\phi)$  from Eq. (8) is greater than 0.5:

987 
$$\mathcal{R}_{\mathcal{A}/\mathcal{E}} = \text{median}_{(t,\phi) \in \text{active}} \left( \frac{E_{k,AeolusHLOS}(t,\phi)}{E_{k,ERA5HLOS}(t,\phi)} \right)$$
 (12)

989 The Ratio-Scaled Energy,  $E_{k,ratio-scaled}$ , is then:

991 
$$E_{k,ratio-scaled}(t, \phi) = \frac{E_{k,AeolusHLOS}(t, \phi)}{\mathcal{R}_{\mathcal{A}/\mathcal{E}}}$$
 (13)

### 992 Step 3: Blending and Final Hovmöller Correction

1002

993 The final corrected Hovmöller field,  $Ek^*(t, \phi)$ , is a weighted average of the two candidates, using the weight map W from Eq. 994 (9):

995 
$$E_k^*(t,\phi) = W(t,\phi) \cdot E_{k,\text{bias-adj}}(t,\phi) + [1 - W(t,\phi)] \cdot E_{k,\text{ratio-scaled}}(t,\phi)$$
 (14)

Any resulting negative values are clipped to zero. The estimated noise component,  $\overline{Ek_{l,N}}$ , as referenced in Eq. (6) of the main text, is therefore equivalent to the total amount subtracted:

98 
$$\overline{Ek_{I.N}} = \overline{Ek_{Aeolus HLOS}} - \overline{Ek_{Aeolus HLOS*}}$$
 (15)

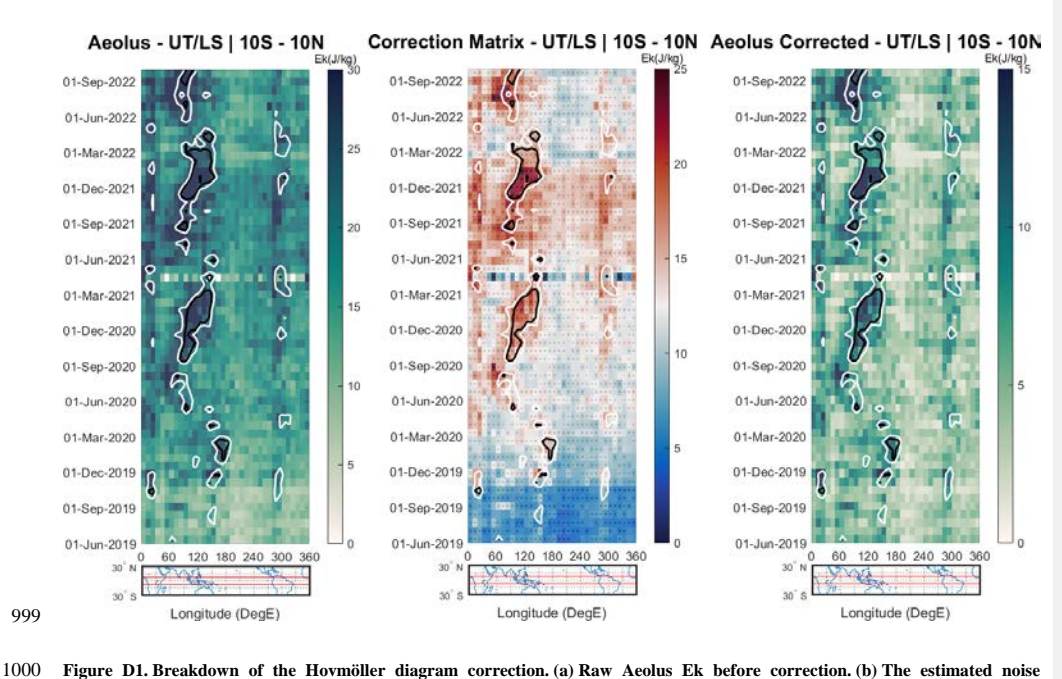


Figure D1. Breakdown of the Hovmöller diagram correction. (a) Raw Aeolus Ek before correction. (b) The estimated noise correction matrix, Ek,I.N. that is subtracted. Note the increasing trend over time, reflecting instrument degradation, and the spatial structure modulated by the blending of additive and multiplicative components. Stippling indicates regions where the corrected

Acolus Ek is statistically different from ERA5. Ek (F-test, p<0.05). (c) Final corrected Acolus Ek (Ek,Hovmöller\*). Background energy levels are significantly reduced while convective hotspots are preserved. White and black contour lines represent 210 and 220 W/m2 OLR, respectively. White contours indicate low Outgoing Longwave radiation (OLR < 220 W/m=2).

Figure D1 illustrates the core steps of the spatio-temporally adaptive noise correction. (a) The raw, uncorrected Aeolus Ek

Hovmöller diagram, showing both geophysical signals and a clear increasing trend in background noise over the mission lifetime. (b) The estimated noise component derived using the adaptive algorithm. Note the temporal increase reflecting instrument degradation, as well as the spatial structure modulated by the blending of additive and multiplicative corrections. (c) The final corrected Aeolus Ek. The background energy levels have been significantly reduced, removing the artificial trend, while the physically meaningful convective hotspots are preserved and sharpened. White contours indicate regions of deep convection (OLR < 220 W m<sup>-2</sup>).

#### 1013 Part 2: Refinement of Noise Correction for Seasonal Geographical Maps

- 1014 For the seasonally averaged geographical maps, which cover a broader latitudinal range (0°S–30°N, denoted by latitude  $\theta$ )
- 1015 than the initial Hovmöller analysis, the noise estimation is refined. For each season (e.g., DJF, MAM, JJA, SON), the estimated
- 1016 noise field from the Hovmöller analysis  $\overline{E}k_{LN}$ , s averaged over the relevant time steps to yield a Seasonal Mean Longitudinal
- 1017 Noise Profile  $\widehat{\widehat{Ek}}_{LN}$ . This yields a seasonally representative longitudinal noise profile. This profile forms the basis for
- 1018 correcting the uncorrected, seasonally-averaged raw Aeolus Ek map,  $E_{k,Aeolus,map}(\theta,\phi)$ . The refinement proceeds in two steps:
- 1019 latitude-weighting and iterative adjustment.

1006

### $1020 \quad \textbf{Step 1: Latitude-Weighting of the Longitudinal Correction} \\$

- 1021 The impact of instrumental noise may be proportionally larger in regions of higher true GW energy. To approximate this, the
- 1022 base longitudinal correction profile is weighted by the latitudinal structure of the raw Aeolus Ek map itself. First, the mean
- 1023 raw Aeolus Ek is calculated for each latitude band,  $E_{k,Aeolus,map}$ . This is normalized to create a latitude weight profile,  $W_0$ :

1024 
$$W_{\theta}(\theta) = \frac{\overline{E_{k,Aeolus,map}(\theta)}}{\max(\overline{E_{k,Aeolus,map}(\theta)})}$$
 (16)

1025 This weight is clipped between 0 and 1. This latitudinal weight is then broadcast across the longitudinal correction profile to 1026 create an initial 2D correction field for the map,  $\Delta E_{map,initial}$ :

1027 
$$\Delta E_{map,initial}(\theta, \phi) = \overline{\hat{E}}_{k,l,N}(\phi) \cdot W_{lat}(\theta)$$
 (17)

### 1028 Step 2: Iterative Adjustment to Prevent Negative Kinetic Energy

- 1029 A simple subtraction of  $\Delta E_{map,initial}$  from  $E_{k,Aeolus,map}$  could result in non-physical negative Ek values where the
- 1030 estimated correction is large relative to the observed Ek. To prevent this, a Columnar Clipping Factor,  $\gamma_{clip}$ , is calculated for
- 1031 each longitude column of the map. This factor is defined as the minimum ratio of the observed energy to the initial correction
- 1032 estimate across all latitudes in that column, ensuring the correction never exceeds the available energy:

1033 
$$\gamma_{clip}(\phi) = \max\left(0, \min\left(1, \min_{\theta} \left[\frac{E_{k,Aeolus,map}(\theta,\phi)}{\Delta E_{map,initial}(\theta,\phi)}\right]\right)\right)$$
 (18)

1034 The final 2D correction field applied to the map is then:

1035 
$$\Delta E_{map,final}(\theta, \phi) = \Delta E_{map,initial}(\theta, \phi) \cdot \gamma_{clip}(\phi)$$
 (19)

### 1036 Step 3: Final Corrected Map and Smoothing

1039

1037 The final corrected seasonal map, denoted as  $\overline{E_{k,AeolusHLOS}^*}$ , is:

1038 
$$\overline{E}_{k,AeolusHLOS}^*(\theta, \phi) = E_{k,Aeolus,map}(\theta, \phi) - \Delta E_{map,final}(\theta, \phi)$$
 (20)

- 1040 Finally, a light 2D spatial smoothing (3x3 moving median followed by a 3x3 moving mean) is applied to the corrected map to
- 1041 reduce pixel-scale noise introduced by the gridding and correction process.

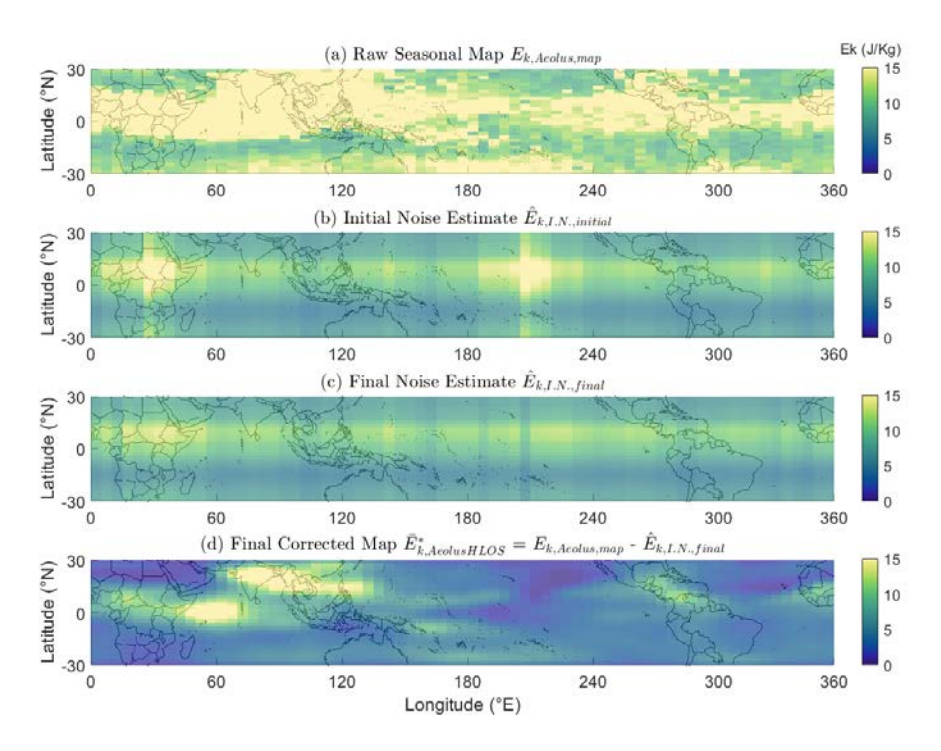


Figure D2. Illustration of the noise correction refinement process for a seasonal geographical map (JJA 2021 shown as an example).

Figure D2 details the refinement steps used to adapt the noise correction for application to 2D seasonal maps. (a) The raw, uncorrected seasonally averaged Aeolus Ek map. (b) The initial noise estimate, created by applying a latitudinal weighting to the seasonal-mean longitudinal noise profile derived from the Hovmöller analysis. (c) The final noise estimate, after an iterative adjustment step that prevents non-physical negative energy values. (d) The final corrected seasonal map, representing the geophysical gravity wave kinetic energy field after the removal of instrumental artifacts. This process ensures that the correction is physically consistent across the entire map domain.

### Diagnostic Validation of Noise Correction

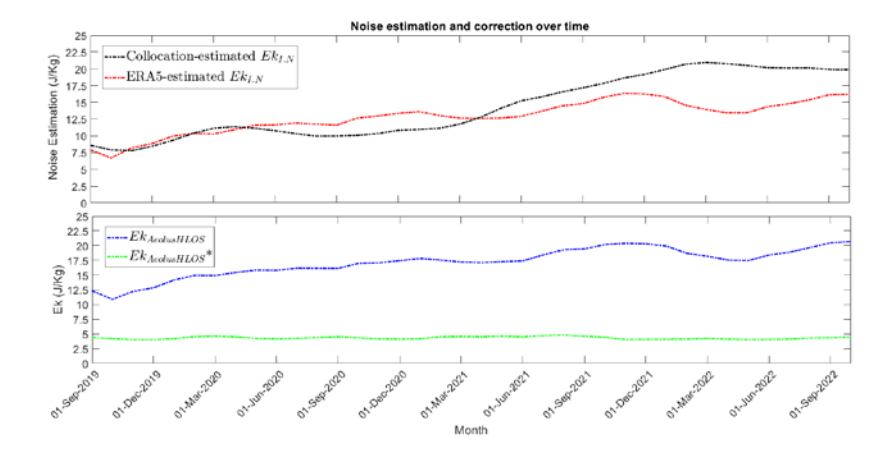


Figure D3. Difference between the Radiosonde-derived (black) and ERA5-derived (red) estimated noise correction, resulting in the difference between the uncorrected Aeolus HLOS GW Ek (blue) and the ERA5-corrected Aeolus HLOS GW Ek (green).

Figure D3 provides an independent validation of the estimated noise trend by comparing the zonally-averaged  $\delta_{noise}(t)$ , term from Eq. (10) with noise estimates derived from collocated radiosonde measurements at La Réunion, as in Ratynski et al. (2023). It is intended to demonstrate that such a method of instrumental noise estimation is qualitatively consistent with the classical approach based on collocated reference measurements applied in (Ratynski et al., 2023).

The Météo-France upper-air soundings in La Réunion (Aéroport Gillot) was used for the conduct of this analysis. For each collocated radiosonde profile with an Aeolus overpass (within 200 km and +/- 6 hours), we downsampled the radiosonde profile resolution to be equivalent to ALADIN vertical bins. A point-wise difference is then calculated, and the standard deviation of these differences is what we refer to as random error. In principle, if Aeolus would not experience any degradation through its systems, this standard deviation would remain stable over the years and periods. However, since we observe an increase, as reported by Ratynski et al. (2023, their Fig.6), a link can be made between the instrument degradation and this increase, wrongly attributing signal-to-noise. Squaring this noise estimation provides a metric homogenous to the observed Ek, representing the repercussions of noise on Ek estimation:

$$Ek_{LN} = \frac{1}{2} \left( \sigma_{Aeolus-Radiosondes} \right)^2$$
 (21)

While both methods provide similar trends, the model approach remains the safest estimation when considering the potential biases.

### 1074 Appendix E: F-Test Ratios

## Aeolus / ERA5 GW Ek | UT/LS | 10S - 10N GNSS-RO / ERA5 Energy Ratio | UT/LS | 10S - 10N

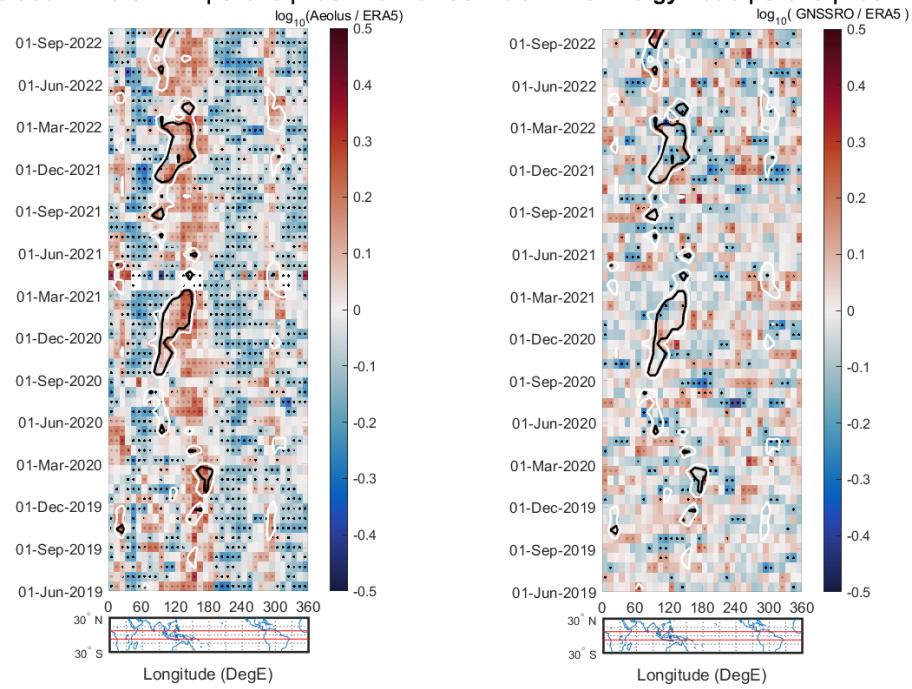


Figure E1. Ratio-based comparison of observed and reanalyzed gravity wave energy for the equatorial band (10°S-10°N), between observational data and ERA5. The UTLS altitudes are defined between one kilometer below the tropopause and 22 km. White and black contour lines represent 210 and 220 W/m2 OLR, respectively. The contour plot represents the Outgoing Longrange Radiation (OLR) for 210 and 220 W/m² (black and white, respectively). Each bin corresponds to an average of over 3 weeks and 10 degrees. The OLR measurements were obtained from the Australian Bureau of Meteorology. The tropopause is determined from the ERA5 reanalysis. The panels show the base-10 logarithm of the ratio between observational data and ERA5.

1083	difference-based analysis. The color scale represents the base-10 logarithm of the ratio, where positive values (red) indicate
1084	that the observational dataset has higher energy than ERA5, and negative values (blue) indicate the opposite.
1085	The first panel reinforces the findings from the main text, showing a systematic and significant overestimation of kinetic energy
1086	by Aeolus relative to ERA5 (predominantly red colors) within the convective regions identified by low OLR. The ratio
1087	frequently exceeds 2 (log <sub>10</sub> ratio > 0.3), particularly over the Indian Ocean and Maritime Continent, confirming that ERA5
1088	substantially underestimates convection-driven kinetic energy.
1089	In contrast to the kinetic energy, the potential energy ratio is much closer to unity ( $log_{10}$ ratio $\approx 0$ ). The colors are predominantly
1090	neutral or light shades of blue/red, indicating that ERA5 and GNSS-RO have very similar magnitudes of potential energy. This
1091	is expected, as ERA5 assimilates GNSS-RO temperature data.
1092	Taken together, these two panels provide evidence for the central conclusion of this study: the discrepancy between
1093	observations and reanalysis is specific to the unassimilated kinetic energy component. While ERA5 successfully reproduces
1094	the potential energy field it is constrained by, it fails to generate the corresponding kinetic energy associated with convection,
1095	a gap that direct wind observations from Aeolus can fill. Black stippling indicates regions where the ratios are statistically
1096	significant (F-test, $p < 0.05$ ).
1097	Data Availability: Aeolus data are publicly available through the Aeolus online dissemination system (https://aeolus-
1098	${\it ds.eo.esa.int/oads/access/)}.  {\it The }  {\it dataset}  {\it used}  {\it for }  {\it the }  {\it realization}  {\it of }  {\it this}  {\it study}  {\it can }  {\it be}  {\it found}  {\it at}  {\it otherwise}  {\it $
1099	https://doi.org/10.5281/zenodo.8113261
1100	
1101	$\textbf{Author Contributions:} \ \ Conceptualization, M.R, S.K, A.H, and M.J.A; methodology, M.R, S.K, A.H, and M.J.A.; software, and M.J.A.; methodology, M.R., S.K., A.H., and M.J.A.; software, and M.J.A.; methodology, M.R., S.K., A.H., and M.J.A.; software, and M.J.A.; methodology, M.R., S.K., A.H., and M.J.A.; software, and M.J.A.; methodology, M.R., S.K., A.H., and M.J.A.; software, and M.J.A.; methodology, M.R., S.K., A.H., and M.J.A.; software, and M.J.A.;$
1102	M.R. and A.M; validation, M.R, S.K, A.H, and M.J.A;—original draft preparation, M.R. and S.K; writing—review and
1103	editing, M.R, S.K, A.H, M.J.A, A.M, P.K and A.M; funding acquisition, S.K, P.K. and A.M; All authors have read and agreed
1104	to the published version of the manuscript.
1105	
1106	Competing interests: The contact author has declared that none of the authors has any competing interests.
1107	
1108	Acknowledgments: The work by Mathieu Ratynski was carried out under a PhD fellowship co-funded by CNES and ACRI-
1109	ST. Additional funding has been provided via the CNES APR Aeolus project. MJA was funded by NSF grants #2110002 and

1082 Figure E1 provides an alternative, ratio-based view of the comparisons presented in the main text, complementing the

1110 #1642644.

#### 1111 References

- 1112 Achatz, U., Alexander, M. J., Becker, E., Chun, H.-Y., Dörnbrack, A., Holt, L., Plougonven, R., Polichtchouk, I., Sato, K.,
- 113 Sheshadri, A., Stephan, C. C., Niekerk, A. van, and Wright, C. J.: Atmospheric Gravity Waves: Processes and
- Parameterization, https://doi.org/10.1175/JAS-D-23-0210.1, 2024.
- 1115 Alexander, M. J. and Ortland, D. A.: Equatorial waves in High Resolution Dynamics Limb Sounder (HIRDLS) data, J.
- 1116 Geophys. Res. Atmospheres, 115, https://doi.org/10.1029/2010JD014782, 2010.
- 1117 Alexander, M. J., Gille, J., Cavanaugh, C., Coffey, M., Craig, C., Eden, T., Francis, G., Halvorson, C., Hannigan, J., Khosravi,
- 1118 R., Kinnison, D., Lee, H., Massie, S., Nardi, B., Barnett, J., Hepplewhite, C., Lambert, A., and Dean, V.: Global estimates of
- 1119 gravity wave momentum flux from High Resolution Dynamics Limb Sounder observations, J. Geophys. Res. Atmospheres,
  - 20 113, https://doi.org/10.1029/2007JD008807, 2008a.
- 1121 Alexander, M. J., Liu, C. C., Bacmeister, J., Bramberger, M., Hertzog, A., and Richter, J. H.: Observational Validation of
- 1122 Parameterized Gravity Waves From Tropical Convection in the Whole Atmosphere Community Climate Model, J. Geophys.
- $123 \quad Res. \ Atmospheres, \ 126, \ e2020 JD 033954, \ https://doi.org/10.1029/2020 JD 033954, \ 2021.$
- 1124 Alexander, S., Tsuda, T., and Kawatani, Y.: COSMIC GPS Observations of Northern Hemisphere winter stratospheric gravity
- 1125 waves and comparisons with an atmospheric general circulation model, Geophys. Res. Lett. GEOPHYS RES LETT, 35,
- 1126 https://doi.org/10.1029/2008GL033174, 2008b.
- 1127 Alexander, S. P., Tsuda, T., and Kawatani, Y.: COSMIC GPS Observations of Northern Hemisphere winter stratospheric
- 1128 gravity waves and comparisons with an atmospheric general circulation model, Geophys. Res. Lett., 35,
  - 29 https://doi.org/10.1029/2008GL033174, 2008c.
- 1130 Alexander, S. P., Tsuda, T., Kawatani, Y., and Takahashi, M.: Global distribution of atmospheric waves in the equatorial upper
- 1131 troposphere and lower stratosphere: COSMIC observations of wave mean flow interactions, J. Geophys. Res. Atmospheres,
- 1132 113, https://doi.org/10.1029/2008JD010039, 2008d.
- 1133 Baker, W. E., Atlas, R., Cardinali, C., Clement, A., Emmitt, G. D., Gentry, B. M., Hardesty, R. M., Källén, E., Kavaya, M. J.,
- 1134 Langland, R., Ma, Z., Masutani, M., McCarty, W., Pierce, R. B., Pu, Z., Riishojgaard, L. P., Ryan, J., Tucker, S., Weissmann,
- 135 M., and Yoe, J. G.: Lidar-Measured Wind Profiles: The Missing Link in the Global Observing System, Bull. Am. Meteorol.
- 1136 Soc., 95, 543–564, https://doi.org/10.1175/BAMS-D-12-00164.1, 2014.
- 1137 Banyard, T. P., Wright, C. J., Hindley, N. P., Halloran, G., Krisch, I., Kaifler, B., and Hoffmann, L.: Atmospheric Gravity
- 1138 Waves in Aeolus Wind Lidar Observations, Geophys. Res. Lett., 48, e2021GL092756,
- 1139 https://doi.org/10.1029/2021GL092756, 2021.
- 1140 Banvard, T. P., Wright, C. J., Osprey, S. M., Hindley, N. P., Halloran, G., Coy, L., Newman, P. A., and Butchart, N.; Aeolus
- wind lidar observations of the 2019/2020 Quasi-Biennial Oscillation disruption with comparison to radiosondes and reanalysis,
- 1142 EGUsphere, 1–23, https://doi.org/10.5194/egusphere-2023-285, 2023.
- 1143 Baumgarten, G., Fiedler, J., Hildebrand, J., and Lübken, F.-J.: Inertia gravity wave in the stratosphere and mesosphere observed
- 1144 by Doppler wind and temperature lidar, Geophys. Res. Lett., 42, 10,929-10,936, https://doi.org/10.1002/2015GL066991, 2015.
- 1145 Bedka, K. M., Velden, C. S., Petersen, R. A., Feltz, W. F., and Mecikalski, J. R.: Comparisons of Satellite-Derived
- 1146 Atmospheric Motion Vectors, Rawinsondes, and NOAA Wind Profiler Observations,
- 1147 https://doi.org/10.1175/2009JAMC1867.1, 2009.

- 1148 Beres, J. H., Garcia, R. R., Boville, B. A., and Sassi, F.: Implementation of a gravity wave source spectrum parameterization
- 1149 dependent on the properties of convection in the Whole Atmosphere Community Climate Model (WACCM), J. Geophys. Res.
- 1150 Atmospheres, 110, https://doi.org/10.1029/2004JD005504, 2005.
- 1151 Bramberger, M., Alexander, M. J., Davis, S., Podglajen, A., Hertzog, A., Kalnajs, L., Deshler, T., Goetz, J. D., and Khaykin,
- 1152 S.: First Super-Pressure Balloon-Borne Fine-Vertical-Scale Profiles in the Upper TTL: Impacts of Atmospheric Waves on
- 1153 Cirrus Clouds and the QBO, Geophys. Res. Lett., 49, e2021GL097596, https://doi.org/10.1029/2021GL097596, 2022.
- 1154 Campos, R. M., Gramcianinov, C. B., de Camargo, R., and da Silva Dias, P. L.: Assessment and Calibration of ERA5 Severe
- 1155 Winds in the Atlantic Ocean Using Satellite Data, Remote Sens., 14, 4918, https://doi.org/10.3390/rs14194918, 2022.
- 1156 Cao, B., Haase, J. S., Murphy, M. J., Alexander, M. J., Bramberger, M., and Hertzog, A.: Equatorial waves resolved by balloon-
- 1157 borne Global Navigation Satellite System radio occultation in the Strateole-2 campaign, Atmospheric Chem. Phys., 22, 15379-
- 1158 15402, https://doi.org/10.5194/acp-22-15379-2022, 2022.
- 1159 Chane Ming, F., Ibrahim, C., Barthe, C., Jolivet, S., Keckhut, P., Liou, Y.-A., and Kuleshov, Y.: Observation and a numerical
- 1160 study of gravity waves during tropical cyclone Ivan (2008), Atmospheric Chem. Phys., 14, 641-658,
- 1161 https://doi.org/10.5194/acp-14-641-2014, 2014.
- 1162 Chen, Q., Ntokas, K., Linder, B., Krasauskas, L., Ern, M., Preusse, P., Ungermann, J., Becker, E., Kaufmann, M., and Riese,
- 163 M.: Satellite observations of gravity wave momentum flux in the mesosphere and lower thermosphere (MLT): feasibility and
- $1164 \quad requirements, Atmospheric Meas. Tech., 15, 7071-7103, \\ https://doi.org/10.5194/amt-15-7071-2022, 2022.$
- 1165 Corcos, M., Bramberger, M., Alexander, M. J., Hertzog, A., Liu, C., and Wright, C.: Observation of Gravity Waves Generated
- 1166 by Convection and the "Moving Mountain" Mechanism During Stratéole-2 Campaigns and Their Impact on the QBO, J.
- 1167 Geophys. Res. Atmospheres, 130, e2024JD041804, https://doi.org/10.1029/2024JD041804, 2025.
- 1168 Danzer, J., Pieler, M., and Kirchengast, G.: Closing the gap in the tropics: the added value of radio-occultation data for wind
- field monitoring across the equator, Atmospheric Meas. Tech. Discuss., 1–19, https://doi.org/10.5194/amt-2023-137, 2023.
- 1170 Dee, D. P.: Bias and data assimilation, Q. J. R. Meteorol. Soc., 131, 3323-3343, https://doi.org/10.1256/qj.05.137, 2005.
- 1171 Dhaka, S. K., Yamamoto, M. K., Shibagaki, Y., Hashiguchi, H., Fukao, S., and Chun, H.-Y.: Equatorial Atmosphere Radar
- observations of short vertical wavelength gravity waves in the upper troposphere and lower stratosphere region induced by
- 1173 localized convection, Geophys. Res. Lett., 33, https://doi.org/10.1029/2006GL027026, 2006.
- 1174 Dzambo, A. M., Hitchman, M. H., and Chang, K.-W.: The Influence of Gravity Waves on Ice Saturation in the Tropical
- 1175 Tropopause Layer over Darwin, Australia, Atmosphere, 10, 778, https://doi.org/10.3390/atmos10120778, 2019.
- 1176 von Engeln, A., Andres, Y., Marquardt, C., and Sancho, F.: GRAS radio occultation on-board of Metop, Adv. Space Res., 47,
- 1177 336–347, https://doi.org/10.1016/j.asr.2010.07.028, 2011.
- 1178 Ern, M., Preusse, P., Alexander, M. J., and Warner, C. D.: Absolute values of gravity wave momentum flux derived from
- 1179 satellite data, J. Geophys. Res. Atmospheres, 109, https://doi.org/10.1029/2004JD004752, 2004.
- 1180 Ern, M., Trinh, Q. T., Preusse, P., Gille, J. C., Mlynczak, M. G., Russell III, J. M., and Riese, M.: GRACILE: a comprehensive
- 1181 climatology of atmospheric gravity wave parameters based on satellite limb soundings, Earth Syst. Sci. Data, 10, 857–892,
- 1182 https://doi.org/10.5194/essd-10-857-2018, 2018.

- 1183 Ern, M., Diallo, M. A., Khordakova, D., Krisch, I., Preusse, P., Reitebuch, O., Ungermann, J., and Riese, M.: The QBO and
- 1184 global-scale tropical waves in Aeolus wind observations, radiosonde data, and reanalyses, EGUsphere, 1-42,
- 185 https://doi.org/10.5194/egusphere-2023-408, 2023.
- 1186 Evan, S., Brioude, J., Rosenlof, K., Davis, S. M., Vömel, H., Héron, D., Posny, F., Metzger, J.-M., Duflot, V., Payen, G.,
- 1187 Vérèmes, H., Keckhut, P., and Cammas, J.-P.: Effect of deep convection on the tropical tropopause layer composition over the
- 1188 southwest Indian Ocean during austral summer, Atmospheric Chem. Phys., 20, 10565–10586, https://doi.org/10.5194/acp-20-
- 1189 10565-2020, 2020.
- 1190 Forbes, J. M., Ern, M., and Zhang, X.: The Global Monsoon Convective System as Reflected in Upper Atmosphere Gravity
- 1191 Waves, J. Geophys. Res. Space Phys., 127, e2022JA030572, https://doi.org/10.1029/2022JA030572, 2022.
- 1192 Fritts, D. C. and Alexander, M. J.: Gravity wave dynamics and effects in the middle atmosphere, Rev. Geophys., 41,
- 1193 https://doi.org/10.1029/2001RG000106, 2003.
- 1194 Fritts, D. C., Wang, L., and Werne, J.: Gravity wave-fine structure interactions: A reservoir of small-scale and large-scale
- turbulence energy, Geophys. Res. Lett., 36, https://doi.org/10.1029/2009GL039501, 2009.
- 1196 Fröhlich, K., Schmidt, T., Ern, M., Preusse, P., de la Torre, A., Wickert, J., and Jacobi, Ch.: The global distribution of gravity
- 1197 wave energy in the lower stratosphere derived from GPS data and gravity wave modelling: Attempt and challenges, J.
- 1198 Atmospheric Sol. Terr. Phys., 69, 2238–2248, https://doi.org/10.1016/j.jastp.2007.07.005, 2007.
- 1199 Geldenhuys, M., Kaifler, B., Preusse, P., Ungermann, J., Alexander, P., Krasauskas, L., Rhode, S., Woiwode, W., Ern, M.,
- 1200 Rapp, M., and Riese, M.: Observations of Gravity Wave Refraction and Its Causes and Consequences, J. Geophys. Res.
- 1201 Atmospheres, 128, e2022JD036830, https://doi.org/10.1029/2022JD036830, 2023.
- 1202 Gubenko, V. N., Pavelyev, A. G., Salimzyanov, R. R., and Andreev, V. E.: A method for determination of internal gravity
- 1203 wave parameters from a vertical temperature or density profile measurement in the Earth's atmosphere, Cosm. Res., 50, 21-
- 1204 31, https://doi.org/10.1134/S0010952512010029, 2012.
- 1205 Guharay, A., Venkat Ratnam, M., Nath, D., and Dumka, U. C.: Investigation of saturated gravity waves in the tropical lower
- 1206 atmosphere using radiosonde observations, Radio Sci., 45, https://doi.org/10.1029/2010RS004372, 2010.
- 1207 Hei, H., Tsuda, T., and Hirooka, T.: Characteristics of atmospheric gravity wave activity in the polar regions revealed by GPS
  - radio occultation data with CHAMP, J. Geophys. Res. Atmospheres, 113, https://doi.org/10.1029/2007JD008938, 2008.
- 1209 Hersbach, H., Bell, B., Berrisford, P., Hirahara, S., Horányi, A., Muñoz-Sabater, J., Nicolas, J., Peubey, C., Radu, R., Schepers,
- 1210 D., Simmons, A., Soci, C., Abdalla, S., Abellan, X., Balsamo, G., Bechtold, P., Biavati, G., Bidlot, J., Bonavita, M., De Chiara,
- 1211 G., Dahlgren, P., Dee, D., Diamantakis, M., Dragani, R., Flemming, J., Forbes, R., Fuentes, M., Geer, A., Haimberger, L.,
- 1212 Healy, S., Hogan, R. J., Hólm, E., Janisková, M., Keeley, S., Laloyaux, P., Lopez, P., Lupu, C., Radnoti, G., de Rosnay, P.,
- 213 Rozum, I., Vamborg, F., Villaume, S., and Thépaut, J.-N.: The ERA5 global reanalysis, Q. J. R. Meteorol. Soc., 146, 1999–
- 1214 2049, https://doi.org/10.1002/qj.3803, 2020.
- 1215 Hindley, N. P., Wright, C. J., Hoffmann, L., Moffat-Griffin, T., and Mitchell, N. J.: An 18-Year Climatology of Directional
- 1216 Stratospheric Gravity Wave Momentum Flux From 3-D Satellite Observations, Geophys. Res. Lett., 47, e2020GL089557,
- 1217 https://doi.org/10.1029/2020GL089557, 2020.
- 218 Huang, K. M., Liu, H., Liu, A. Z., Zhang, S. D., Huang, C. M., Gong, Y., and Ning, W. H.: Investigation on Spectral
- 1219 Characteristics of Gravity Waves in the MLT Using Lidar Observations at Andes, J. Geophys. Res. Space Phys., 126,
- 1220 e2020JA028918, https://doi.org/10.1029/2020JA028918, 2021.

- John, S. R. and Kumar, K. K.: A discussion on the methods of extracting gravity wave perturbations from space-based
- measurements, Geophys. Res. Lett., 40, 2406–2410, https://doi.org/10.1002/grl.50451, 2013.
- 1223 Kalisch, S., Chun, H.-Y., Ern, M., Preusse, P., Trinh, Q. T., Eckermann, S. D., and Riese, M.: Comparison of simulated and
- 1224 observed convective gravity waves, J. Geophys. Res. Atmospheres, 121, 13,474-13,492
- 1225 https://doi.org/10.1002/2016JD025235, 2016.
- 1226 Kang, M.-J., Chun, H.-Y., and Kim, Y.-H.: Momentum Flux of Convective Gravity Waves Derived from an Offline Gravity
- 1227 Wave Parameterization. Part I: Spatiotemporal Variations at Source Level, https://doi.org/10.1175/JAS-D-17-0053.1, 2017.
- 1228 Khaykin, S. M., Hauchecorne, A., Mzé, N., and Keckhut, P.: Seasonal variation of gravity wave activity at midlatitudes from
- 1229 7 years of COSMIC GPS and Rayleigh lidar temperature observations, Geophys. Res. Lett., 42, 1251-1258,
- 1230 https://doi.org/10.1002/2014GL062891, 2015.
- 1231 Krisch, I., Hindley, N. P., Reitebuch, O., and Wright, C. J.: On the derivation of zonal and meridional wind components from
- $1232 \quad Aeolus \ horizontal \ line-of-sight \ wind, \ Atmospheric \ Meas. \ Tech., \ 15, \ 3465-3479, \ https://doi.org/10.5194/amt-15-3465-2022, \ https$
- 1233 2022
- 1234 Kruse, C. G., Richter, J. H., Alexander, M. J., Bacmeister, J. T., Heale, C., and Wei, J.: Gravity Wave Drag Parameterizations
- 1235 for Earth's Atmosphere, in: Fast Processes in Large-Scale Atmospheric Models, American Geophysical Union (AGU), 229-
- 1236 256, https://doi.org/10.1002/9781119529019.ch9, 2023.
- 1237 Kumari, K., Wu, H., Long, A., Lu, X., and Oberheide, J.: Mechanism Studies of Madden-Julian Oscillation Coupling Into the
- 1238 Mesosphere/Lower Thermosphere Tides Using SABER, MERRA-2, and SD-WACCMX, J. Geophys. Res. Atmospheres, 126,
- 1239 e2021JD034595, https://doi.org/10.1029/2021JD034595, 2021.
- 1240 Kursinski, E. R., Hajj, G. A., Schofield, J. T., Linfield, R. P., and Hardy, K. R.: Observing Earth's atmosphere with radio
- 1241 occultation measurements using the Global Positioning System, J. Geophys. Res. Atmospheres, 102, 23429-23465,
- 1242 https://doi.org/10.1029/97JD01569, 1997.
- 1243 Ladstädter, F., Steiner, A. K., Foelsche, U., Haimberger, L., Tavolato, C., and Kirchengast, G.: An assessment of differences
- 1244 in lower stratospheric temperature records from (A)MSU, radiosondes, and GPS radio occultation, Atmospheric Meas. Tech.,
- 1245 4, 1965–1977, https://doi.org/10.5194/amt-4-1965-2011, 2011.
- 1246 Liu, C., Alexander, J., Richter, J., and Bacmeister, J.: Using TRMM Latent Heat as a Source to Estimate Convection Induced
- 1247 Gravity Wave Momentum Flux in the Lower Stratosphere, J. Geophys. Res. Atmospheres, 127, e2021JD035785,
- 1248 https://doi.org/10.1029/2021JD035785, 2022.
- 1249 Luna, D., Alexander, P., and de la Torre, A.: Evaluation of uncertainty in gravity wave potential energy calculations through
- 1250 GPS radio occultation measurements, Adv. Space Res., 52, 879–882, https://doi.org/10.1016/j.asr.2013.05.015, 2013.
- 1251 Lux, O., Witschas, B., Geiß, A., Lemmerz, C., Weiler, F., Marksteiner, U., Rahm, S., Schäfler, A., and Reitebuch, O.: Quality
- 1252 control and error assessment of the Aeolus L2B wind results from the Joint Aeolus Tropical Atlantic Campaign, Atmospheric
- 253 Meas. Tech., 15, 6467–6488, https://doi.org/10.5194/amt-15-6467-2022, 2022.
- 1254 Mack, L. R. and Jay, B. E.: The partition of energy in standing gravity waves of finite amplitude, J. Geophys. Res. 1896-1977,
- 1255 72, 573–581, https://doi.org/10.1029/JZ072i002p00573, 1967.
- 1256 MARQUARDT, C. and Healy, S.: Measurement Noise and Stratospheric Gravity Wave Characteristics Obtained from GPS
- 257 Occultation Data, J. Meteorol. Soc. Jpn. J METEOROL SOC JPN, 83, 417–428, https://doi.org/10.2151/jmsj.83.417, 2005.

Mis en forme : Espagnol (Amérique latine)

- 1258 Munday, C., Engelstaedter, S., Ouma, G., Ogutu, G., Olago, D., Ong'ech, D., Lees, T., Wanguba, B., Nkatha, R., Ogolla, C.,
- 1259 Gàlgalo, R. A., Dokata, A. J., Kirui, E., Hope, R., and Washington, R.: Observations of the Turkana Jet and the East African
- 1260 Dry Tropics: The RIFTJet Field Campaign, Bull. Am. Meteorol. Soc., 103, E1828–E1842, https://doi.org/10.1175/BAMS-D-
- 1261 21-0214.1, 2022.
- 1262 Muñoz-Sabater, J., Dutra, E., Agustí-Panareda, A., Albergel, C., Arduini, G., Balsamo, G., Boussetta, S., Choulga, M.,
- 1263 Harrigan, S., Hersbach, H., Martens, B., Miralles, D. G., Piles, M., Rodríguez-Fernández, N. J., Zsoter, E., Buontempo, C.,
- 1264 and Thépaut, J.-N.: ERA5-Land: a state-of-the-art global reanalysis dataset for land applications, Earth Syst. Sci. Data, 13,
- 1265 4349-4383, https://doi.org/10.5194/essd-13-4349-2021, 2021.
- 1266 Nastrom, G. D., Hansen, A. R., Tsuda, T., Nishida, M., and Ware, R.: A comparison of gravity wave energy observed by VHF
- 1267 radar and GPS/MET over central North America, J. Geophys. Res. Atmospheres, 105, 4685-4687,
- 1268 https://doi.org/10.1029/1999JD901164, 2000.
- 1269 Orr, A., Bechtold, P., Scinocca, J., Ern, M., and Janiskova, M.: Improved Middle Atmosphere Climate and Forecasts in the
- 1270 ECMWF Model through a Nonorographic Gravity Wave Drag Parameterization, https://doi.org/10.1175/2010JCLI3490.1,
- 1271 2010
- 1272 Pahlavan, H. A., Fu, Q., Wallace, J. M., and Kiladis, G. N.: Revisiting the Quasi-Biennial Oscillation as Seen in ERA5. Part
- 273 I: Description and Momentum Budget, https://doi.org/10.1175/JAS-D-20-0248.1, 2021.
- 1274 Plougonven, R. and Zhang, F.: Internal gravity waves from atmospheric jets and fronts, Rev. Geophys., 52, 33-76,
- 1275 https://doi.org/10.1002/2012RG000419, 2014.
- 1276 Plougonven, R., Jewtoukoff, V., Cámara, A. de la, Lott, F., and Hertzog, A.: On the Relation between Gravity Waves and
- 1277 Wind Speed in the Lower Stratosphere over the Southern Ocean, https://doi.org/10.1175/JAS-D-16-0096.1, 2017.
- 1278 Podglaien, A., Hertzog, A., Plougonyen, R., and Žagar, N.: Assessment of the accuracy of (re)analyses in the equatorial lower
- 1279 stratosphere, J. Geophys. Res. Atmospheres, 119, 11,166-11,188, https://doi.org/10.1002/2014JD021849, 2014.
- 1280 Randel, W. J. and Wu, F.: Kelvin wave variability near the equatorial tropopause observed in GPS radio occultation
- 1281 measurements, J. Geophys. Res. Atmospheres, 110, https://doi.org/10.1029/2004JD005006, 2005.
- 1282 Randel, W. J., Wu, F., and Podglajen, A.: Equatorial Waves, Diurnal Tides and Small-Scale Thermal Variability in the Tropical
- 1283 Lower Stratosphere From COSMIC-2 Radio Occultation, J. Geophys. Res. Atmospheres, 126, e2020JD033969,
- 1284 https://doi.org/10.1029/2020JD033969, 2021.
- 1285 Ratynski, M., Khaykin, S., Hauchecorne, A., Wing, R., Cammas, J.-P., Hello, Y., and Keckhut, P.: Validation of Aeolus wind
- 1286 profiles using ground-based lidar and radiosonde observations at Réunion island and the Observatoire de Haute-Provence,
- 1287 Atmospheric Meas. Tech., 16, 997–1016, https://doi.org/10.5194/amt-16-997-2023, 2023.
- 1288 The NWP impact of Aeolus Level-2B winds at ECMWF: https://www.ecmwf.int/en/elibrary/81546-nwp-impact-aeolus-level-
- 1289 2b-winds-ecmwf, last access: 28 June 2025.
- 1290 Rennie, M. P., Isaksen, L., Weiler, F., Jos de Kloe, Kanitz, T., and Reitebuch, O.: The impact of Aeolus wind retrievals on
- 1291 ECMWF global weather forecasts, Q. J. R. Meteorol. Soc., 147, 3555–3586, https://doi.org/10.1002/qj.4142, 2021.
- 1292 Šácha, P., Foelsche, U., and Pišoft, P.: Analysis of internal gravity waves with GPS RO density profiles, Atmospheric Meas.
- Tech., 7, 4123–4132, https://doi.org/10.5194/amt-7-4123-2014, 2014.

- 1294 Schmidt, T., de la Torre, A., and Wickert, J.: Global gravity wave activity in the tropopause region from CHAMP radio
- 1295 occultation data, Geophys. Res. Lett., 35, https://doi.org/10.1029/2008GL034986, 2008.
- 1296 Schmidt, T., Alexander, P., and de la Torre, A.: Stratospheric gravity wave momentum flux from radio occultations, J.
- 1297 Geophys. Res. Atmospheres, 121, 4443–4467, https://doi.org/10.1002/2015JD024135, 2016.
- 1298 Scinocca, J. F.: An Accurate Spectral Nonorographic Gravity Wave Drag Parameterization for General Circulation Models,
- 1299 2003.
- 1300 Stephan, C. C. and Mariaccia, A.: The signature of the tropospheric gravity wave background in observed mesoscale motion,
- 1301 Weather Clim. Dyn., 2, 359–372, https://doi.org/10.5194/wcd-2-359-2021, 2021.
- 1302 Stephan, C. C., Zagar, N., and Shepherd, T. G.: Waves and coherent flows in the tropical atmosphere: new opportunities, old
- 1303 challenges, Q. J. R. Meteorol. Soc., 147, 2597–2624, https://doi.org/10.1002/qj.4109, 2021.
- 1304 Tsuda, T., Nishida, M., Rocken, C., and Ware, R. H.: A Global Morphology of Gravity Wave Activity in the Stratosphere
- 1305 Revealed by the GPS Occultation Data (GPS/MET), J. Geophys. Res. Atmospheres, 105, 7257–7273,
- 1306 https://doi.org/10.1029/1999JD901005, 2000.
- 1307 Tsuda, T., Ratnam, M. V., May, P. T., Alexander, M. J., Vincent, R. A., and MacKinnon, A.: Characteristics of gravity waves
- 1308 with short vertical wavelengths observed with radiosonde and GPS occultation during DAWEX (Darwin Area Wave
- 1309 Experiment), J. Geophys. Res. Atmospheres, 109, https://doi.org/10.1029/2004JD004946, 2004.
- 1310 VanZandt, T. E.: A model for gravity wave spectra observed by Doppler sounding systems, Radio Sci., 20, 1323-1330,
- 1311 https://doi.org/10.1029/RS020i006p01323, 1985.
- 1312 Waite, M. L. and Snyder, C.: The Mesoscale Kinetic Energy Spectrum of a Baroclinic Life Cycle,
- 1313 https://doi.org/10.1175/2008JAS2829.1, 2009.
- 1314 Wang, L. and Alexander, M. J.: Global estimates of gravity wave parameters from GPS radio occultation temperature data, J.
- 1315 Geophys. Res. Atmospheres, 115, https://doi.org/10.1029/2010JD013860, 2010.
- 1316 Weiler, F., Kanitz, T., Wernham, D., Rennie, M., Huber, D., Schillinger, M., Saint-Pe, O., Bell, R., Parrinello, T., and
- 1317 Reitebuch, O.: Characterization of dark current signal measurements of the ACCDs used on board the Aeolus satellite,
- 1318 Atmospheric Meas. Tech., 14, 5153–5177, https://doi.org/10.5194/amt-14-5153-2021, 2021.
- 1319 Wing, R., Strelnikova, I., Dörnbrack, A., Gerding, M., Franco-Diaz, E., Holt, L., Mossad, M., and Baumgarten, G.: Direct
- 1320 Observation of Quasi-Monochromatic Gravity Wave Packets Associated With the Polar Night Jet Using a Doppler-Rayleigh
- 1321 Lidar, J. Geophys. Res. Atmospheres, 130, e2025JD043707, https://doi.org/10.1029/2025JD043707, 2025.
- 1322 Woiwode, W., Dörnbrack, A., Geldenhuys, M., Friedl-Vallon, F., Giez, A., Gulde, T., Höpfner, M., Johansson, S., Kaifler, B.,
- 1323 Kleinert, A., Krasauskas, L., Kretschmer, E., Maucher, G., Neubert, T., Nordmeyer, H., Piesch, C., Preusse, P., Rapp, M.,
- 1324 Riese, M., Schumann, U., and Ungermann, J.: Non-Orographic Gravity Waves and Turbulence Caused by Merging Jet
- 1325 Streams, J. Geophys. Res. Atmospheres, 128, e2022JD038097, https://doi.org/10.1029/2022JD038097, 2023.
- 1326 Wright, C. J. and Gille, J. C.: HIRDLS observations of gravity wave momentum fluxes over the monsoon regions, J. Geophys.
- 1327 Res. Atmospheres, 116, https://doi.org/10.1029/2011JD015725, 2011.
- 1328 Wright, C. J. and Hindley, N. P.: How well do stratospheric reanalyses reproduce high-resolution satellite temperature
- 1329 measurements?, Atmospheric Chem. Phys., 18, 13703–13731, https://doi.org/10.5194/acp-18-13703-2018, 2018.

- 1330 Wright, C. J., Ungermann, J., Preusse, P., and Polichtchouk, I.: Using sub-limb observations to measure gravity waves excited
- 1331 by convection, Npj Microgravity, 9, 14, https://doi.org/10.1038/s41526-023-00259-2, 2023.
- 1332 Wüst, S. and Bittner, M.: Gravity wave reflection: Case study based on rocket data, J. Atmospheric Sol.-Terr. Phys., 70, 742-
- 1333 755, https://doi.org/10.1016/j.jastp.2007.10.010, 2008.
- 1334 Yang, S.-S., Pan, C.-J., and Das, U.: Investigating the Spatio-Temporal Distribution of Gravity Wave Potential Energy over
- 1335 the Equatorial Region Using the ERA5 Reanalysis Data, Atmosphere, 12, 311, https://doi.org/10.3390/atmos12030311, 2021.
- 1336 Žagar, N., Gustafsson, N., and Källén, E.: Variational data assimilation in the tropics: The impact of a background-error
- 1337 constraint, Q. J. R. Meteorol. Soc., 130, 103–125, https://doi.org/10.1256/qj.03.13, 2004.
- 1338 Žagar, N., Rennie, M., and Isaksen, L.: Uncertainties in Kelvin Waves in ECMWF Analyses and Forecasts: Insights From
- 1339 Aeolus Observing System Experiments, Geophys. Res. Lett., 48, e2021GL094716, https://doi.org/10.1029/2021GL094716,
- 1340 2021
- 1341 Žagar, N., Pilch Kedzierski, R., De Chiara, G., Healy, S., Rennie, M., and Sielmann, F.: ESA's Aeolus Mission Reveals
- 1342 Uncertainties in Tropical Wind and Wave-Driven Circulations, Geophys. Res. Lett., 52, e2025GL114832,
- 1343 https://doi.org/10.1029/2025GL114832, 2025.
- 1344 Zhang, J., Guo, J., Xue, H., Zhang, S., Huang, K., Dong, W., Shao, J., Yi, M., and Zhang, Y.: Tropospheric Gravity Waves as
- 1345 Observed by the High-Resolution China Radiosonde Network and Their Potential Sources, J. Geophys. Res. Atmospheres,
- 1346 127, e2022JD037174, https://doi.org/10.1029/2022JD037174, 2022.
- 1347 Zhang, K., Randel, W. J., and Fu, R.: Relationships between outgoing longwave radiation and diabatic heating in reanalyses,
- 1348 Clim. Dyn., 49, 2911–2929, https://doi.org/10.1007/s00382-016-3501-0, 2017.
- 1349 Zhang, S. D. and Yi, F.: A statistical study of gravity waves from radiosonde observations at Wuhan (30° N, 114° E) China,
- 1350 Ann. Geophys., 23, 665–673, https://doi.org/10.5194/angeo-23-665-2005, 2005.
- 1351 Zhang, S. D., Yi, F., Huang, C. M., and Zhou, Q.: Latitudinal and seasonal variations of lower atmospheric inertial gravity
- 1352 wave energy revealed by US radiosonde data, Ann. Geophys., 28, 1065-1074, https://doi.org/10.5194/angeo-28-1065-2010,
- 1353 2010.

1354